



# A very high-order finite volume method for hyperbolic systems: Multi-dimensional Optimal Order Detection (MOOD).

Stéphane Clain, Steven Diot, Raphaël Loubère

## ► To cite this version:

Stéphane Clain, Steven Diot, Raphaël Loubère. A very high-order finite volume method for hyperbolic systems: Multi-dimensional Optimal Order Detection (MOOD).. 2010. hal-00518478v1

**HAL Id: hal-00518478**

**<https://hal.science/hal-00518478v1>**

Preprint submitted on 17 Sep 2010 (v1), last revised 15 Feb 2011 (v2)

**HAL** is a multi-disciplinary open access archive for the deposit and dissemination of scientific research documents, whether they are published or not. The documents may come from teaching and research institutions in France or abroad, or from public or private research centers.

L'archive ouverte pluridisciplinaire **HAL**, est destinée au dépôt et à la diffusion de documents scientifiques de niveau recherche, publiés ou non, émanant des établissements d'enseignement et de recherche français ou étrangers, des laboratoires publics ou privés.

# A very high-order finite volume method for hyperbolic systems: Multi-dimensional Optimal Order Detection (MOOD).

S. Clain <sup>a,b</sup>, S. Diot <sup>a</sup>, R. Loubère <sup>a</sup>

<sup>a</sup>*Institut de Mathématiques de Toulouse, Université de Toulouse, France*

<sup>b</sup>*Departamento de Matemática e Aplicações Campus de Gualtar - 4710-057 Braga  
Campus de Azurm - 4800-058 Guimares, Portugal*

---

## Abstract

In this paper, we investigate a new way to deal with the problems generated by the limitation process of very high-order finite volume methods based on polynomial reconstructions. Multi-dimensional Optimal Order Detection (MOOD) breaks away from classical limitations employed in MUSCL or ENO/WENO. Indeed, instead of classical limiting of polynomial reconstructions, MOOD detects problematic situations after each time evaluation of the solution. Then, locally, the flux approximations are modified by reducing the local polynomial degree and the solution is updated. Several advantages are consequently gained: the concept is simple, totally independent of mesh structure in any spatial dimension and is able to take physics into account thanks to its “a posteriori” detection. The detection uses the Discrete Maximum Principle (DMP) for advection problem. For Euler system the detection is based on a mix between DMP on density variable and positivity of pressure. In order to avoid expensive substeps of polynomial limiting the solution re-evaluations are embedded into the substeps of a Runge-Kutta high-order time discretization. Numerical results on classical and demanding tests cases are proposed on quadrangular meshes to support the promising potential of this approach.

*Key words:* Finite Volume, high-order, conservation law, MUSCL, polynomial reconstruction, limitation, MOOD.

---

---

*Email addresses:* `stephane.clain@math.univ-toulouse.fr` (S. Clain),  
`steven.diot@math.univ-toulouse.fr` (S. Diot),  
`raphael.loubere@math.univ-toulouse.fr` (R. Loubère).

## 1 Introduction

High-order methods for system of nonlinear conservation laws are an important challenging question with a wide range of applications. Since four decades numerical schemes have been designed to be used in simulation codes in order to accurately approach these solutions on a computational mesh. Today engineering community has to deal with complex domains as the computational power increases. Consequently the meshes that are employed are at minimum heterogeneous, often unstructured and sometimes non-conformal. Therefore new numerical methods must be designed to deal with highly stretched mesh made of different cell shapes (as instance in two dimensions such mesh is built with triangles, quadrangles, polygons mixed together and eventually degenerated). In three dimensions the situation becomes even more complex as the mesh generation is not a trivial task.

The Finite Volume (FV) method is a very popular technique due to its simplicity since only one unknown located at cell center is carried out, and, its build-in conservativity property. FV became very popular and nowadays many engineering applications or commercial codes are based on a finite volume formulation. The major drawback of a direct use of the FV method is the presence of a large amount of numerical diffusion leading to a poor accuracy and over smoothed shock waves. To overcome such a problem, high-order methods such as MUSCL [39], PPM [15], (W)ENO [19,20] or ADER [35] techniques based on a local polynomial reconstruction allow to increase the spatial approximation accuracy and consequently reduce the numerical diffusion. The main difficulty of all these approaches is that a simple polynomial reconstruction is not enough to obtain an accurate and physically relevant solution free of spurious oscillations. The schemes coupled with a reconstruction technique have to respect an important property: the Discrete Maximum Principle to ensure  $L^\infty$  stability for the scalar autonomous hyperbolic problem [3,6,8–10]. Such a constraint also holds for systems where non-physical oscillations and non-physical solutions have to be eliminated. The goal of high-order accurate numerical approximations is such that they achieve high accuracy on smooth regions and sharpen profiles of discontinuities, without spurious oscillations. Many authors have contributed to increase the numerical scheme performance still maintaining a reasonable computational cost. Several methods are relatively well-defined such as:

- the MUSCL method [39,3,4,6,10,21,27],
- the PPM [15,7],
- the ENO/WENO method [1,22,26,32,33,42,44],
- the spectral method [18,40,41],
- the residual distribution method [2,16,28],
- the ADER methods [35,37,17],
- the Discontinuous Galerkin method [11–14].

The MUSCL method [39] is probably the most popular high-order FV method. Spatial second-order accurate schemes usually use piecewise linear polynomial reconstruction. This reconstruction is equipped with a limiter that reduces the accuracy to first-order near discontinuities and steep gradients in order to ensure the stability of the overall scheme. The choice of the limiter has been extensively discussed and some popular limiters each with specific qualities and drawbacks are today available (minmod, superbee, Van Leer, Barth-Jespersen [4] for instance). A second-order in time discretization is employed to get a formally second-order scheme away from discontinuity.

More advanced schemes using polynomial reconstructions emerged with PPM. It is widely used in many operational codes (gas dynamics, astrophysics, relativity, meteorological simulation). However it is only an upwind biased method meaning that its multidimensional extension never requires any multidimensional polynomial reconstruction. Only 1D parabolic state variable reconstructions are performed in the canonical directions. Monotonicity is ensured by a limiting process inspired from the slope limitation of MUSCL method. Essentially non oscillatory (ENO) polynomial reconstruction procedures were designed to reach “very” high-order accuracy [19,20,1,33,32]. As quoted in [25]: *The ENO concept represents an extension of the Godunov approach based upon higher order reconstruction of the solution, in a similar way to the MUSCL and PPM schemes, but using an adaptive stencil that ensures that information is always obtained from smooth regions of the flow.* This procedure starts from a piecewise constant description of physical variable. Then the naive ENO method reconstructs any possible polynomial of user-given degree using any possible local stencil. Amongst all of them the least oscillatory polynomial is chosen and further used by the numerical scheme. ENO schemes can retain high-order spatial accuracy even at points of extrema, by allowing accentuation of local extrema, which, in other words, means that the Discrete Maximum Principle may be violated. Some additional operations are involved in polynomial computations. Moreover extra difficulties and complexities have to be faced for the implementation on multidimensional unstructured grids [5]. These drawbacks finally disqualify ENO type of method within our context. Contrarily to the previous methods the Discontinuous Galerkin (DG) method [11–14] carry several unknowns per variable per cell. The polynomial coefficients used to describe one variable in a given cell are solved rather than reconstructed. Usually they are the mean value and some representation of first, second and higher derivatives. A limiter has still to be designed and has to be used to ensure monotonicity and physically relevant approximation.

In the present paper, we propose a new strategy to develop very high-order schemes within a Finite Volume Eulerian framework. These new schemes use polynomial reconstructions of state variables as for MUSCL and ENO methods and they strictly preserve the Discrete Maximum Principle. The efficiency relies on a Multi-dimensional Optimal Order Detection (MOOD). In each cell this optimal order is used to build the numerical flux that leads to the preservation of the maximum principle. At each time step, the MOOD method

consists in an iterative procedure where we first initialize all the local polynomial reconstructions to a maximum degree that we further decrement up to satisfaction of the Discrete Maximum Principle. Instead of designing an *a priori* limiter as for any MUSCL/ENO/DG like techniques one reduces the polynomial degree *a posteriori*. The iterative decrementing procedure is in fact embedded in the sub-steps of a Runge-Kutta scheme leading to a high-order time discretization.

The paper is organized as follows. Section 2 is dedicated to the generic framework used to describe the MOOD method where the high-order finite volume scheme is presented. Section 3 is devoted to the polynomial reconstruction and to a short presentation of the classical limiting procedure used in the MUSCL method. The MOOD method is detailed in the fourth section where we introduce the two fundamental notions: Cell Polynomial Degree and Edge Polynomial Degree. We present several strategies to decrement and evaluate the reconstructed values employed to compute the numerical flux. We extend the MOOD method to vectorial value problem such as the Euler system in section 5. At last, in sections 6 and 7 are gathered the numerical results for scalar and vectorial values problems respectively. The convergence rates are studied and the maximum principle preservation is verified. Classical tests are carried out for the scalar and Euler hyperbolic system of conservation laws. Comparisons with an existing MUSCL method are provided and prove the efficiency of the MOOD method. The last section gathers conclusion and perspectives.

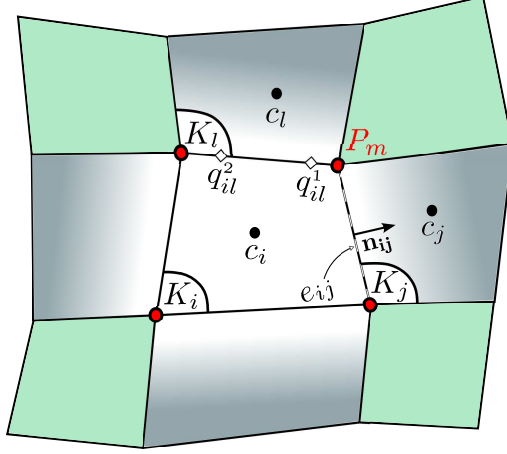


Fig. 1. Mesh notation.  $K_i$  is a generic element with the centroid  $c_i$ . Index set  $\underline{\nu}(i)$  corresponds to blue cells (with gradation),  $\overline{\nu}(i)$  corresponds to every non-white cells and  $\lambda(i)$  is the set of red  $P_m$  node indexes. Edges are denoted by  $e_{ij}$  with  $\mathbf{n}_{ij}$  the unit outward normal vector of element  $K_i$ . Numerical integration on edge  $e_{il}$  is performed with the two Gauss points  $q_{il}^1, q_{il}^2$ .

## 2 General framework

We consider the generic scalar hyperbolic equation defined on a domain  $\Omega \subset \mathbb{R}^2$ ,  $t > 0$  cast in the conservative form

$$\partial_t u + \nabla \cdot F(u) = 0, \quad (1a)$$

$$u(\cdot, 0) = u_0, \quad (1b)$$

where  $\mathbf{x} = (x_1, x_2)$  denotes a point of  $\Omega$  and  $t$  the time,  $u = u(\mathbf{x}, t)$  is the unknown function,  $F = (f_1, f_2)$  is the physical flux and  $u_0$  is the initial condition. Boundary conditions shall be prescribed in the following.

To elaborate the discretization in time and space, we introduce the following ingredients. We assume that the computation domain  $\Omega$  is a polygonal bounded set of  $\mathbb{R}^2$  divided into quadrangles  $K_i$ ,  $i \in \mathcal{E}_{el}$  where  $\mathcal{E}_{el}$  is the cell index set. For each cell  $K_i$ ,  $\lambda(i)$  is the set of all the nodes  $P_m$ ,  $m \in \lambda(i)$  while  $e_{ij}$  denotes the common edge between  $K_i$  and  $K_j$  with  $j \in \underline{\nu}(i)$ ,  $\underline{\nu}(i)$  being the index set of all the elements which share a common side with  $K_i$ . Moreover,  $\overline{\nu}(i)$  represents the index set of all  $K_j$  such that  $K_i \cap K_j \neq \emptyset$  (see figure 1). At last,  $|K_i|$  and  $|e_{ij}|$  measure the surface of  $K_i$  and the length of  $e_{ij}$  respectively.

To compute an approximation of the solution of equation (1), we first integrate formally in time between  $t^n$  and  $t^{n+1}$  and in space over a cell  $K_i$

$$\int_{t^n}^{t^{n+1}} \int_{K_i} \partial_t u(\mathbf{x}, t) d\mathbf{x} dt + \int_{t^n}^{t^{n+1}} \int_{K_i} \nabla \cdot F(u(\mathbf{x}, t)) d\mathbf{x} dt = 0, \quad (2)$$

the previous equation can be rewritten assuming function  $u$  regular enough into

$$\int_{t^n}^{t^{n+1}} \partial_t \left( \int_{K_i} u(\mathbf{x}, t) d\mathbf{x} \right) dt + \int_{t^n}^{t^{n+1}} \int_{\partial K_i} F(u(\mathbf{s}, t)) \cdot \mathbf{n}_{ij} ds dt = 0, \quad (3)$$

where the cell boundary  $\partial K_i$  is the union edges  $e_{ij}$ ,  $j \in \mathcal{V}(i)$ ,  $d\mathbf{s}$  is the length element along  $\partial K_i$  and  $\mathbf{n}_{ij}$  the unit normal vector of  $e_{ij}$  from  $K_i$  toward  $K_j$ . Finally evaluating the first term yields

$$\int_{K_i} u(\mathbf{x}, t^{n+1}) d\mathbf{x} - \int_{K_i} u(\mathbf{x}, t^n) d\mathbf{x} + \sum_{j \in \mathcal{V}(i)} \int_{t^n}^{t^{n+1}} \int_{e_{ij}} F(u(\mathbf{s}, t)) \cdot \mathbf{n}_{ij} ds dt = 0. \quad (4)$$

Let us introduce an approximate mean value of  $u$  on  $K_i$  at any time  $t^n$

$$u_i^n \simeq \left\langle u(\mathbf{x}, t^n) \right\rangle_{K_i} = \frac{1}{|K_i|} \int_{K_i} u(\mathbf{x}, t^n) d\mathbf{x}, \quad (5)$$

and the numerical flux between  $K_i$  and  $K_j$  evaluated at  $t^n$  as

$$G_{ij}^n \simeq \frac{1}{|e_{ij}|} \int_{e_{ij}} F(u(\mathbf{s}, t^n)) \cdot \mathbf{n}_{ij} d\mathbf{s}. \quad (6)$$

An explicit scheme to solve (4) writes

$$u_i^{n+1} = u_i^n - \Delta t \sum_{j \in \mathcal{V}(i)} \frac{|e_{ij}|}{|K_i|} G_{ij}^n, \quad (7)$$

where  $\Delta t = t^{n+1} - t^n$ . More precisely a generic first order explicit finite volume scheme writes

$$u_i^{n+1} = u_i^n - \Delta t \sum_{j \in \mathcal{V}(i)} \frac{|e_{ij}|}{|K_i|} G(u_i^n, u_j^n, \mathbf{n}_{ij}), \quad (8)$$

where  $G_{ij} = G(u_i^n, u_j^n, \mathbf{n}_{ij})$  is a numerical flux which satisfies the classical properties of consistency and monotonicity. Unfortunately, such a scheme only provides first-order accuracy in space and higher-order reconstruction techniques are used to improve the solution approximation.

To this end, we substitute in equation (8) the first-order approximation  $u_i^n$  and  $u_j^n$  with better approximations of  $u_{ij,r}^n$  on the  $e_{ij}$  edge. Consequently numerical integration on the boundary of  $K_i$  in (6) has to be performed with enough accuracy which is obtained by using high-order quadrature formula. Indeed, we consider the generic high-order finite volume scheme

$$u_i^{n+1} = u_i^n - \Delta t \sum_{j \in \mathcal{V}(i)} \frac{|e_{ij}|}{|K_i|} \sum_{r=1}^R \xi_r G(u_{ij,r}^n, u_{ji,r}^n, \mathbf{n}_{ij}), \quad (9)$$

where  $u_{ij,r}^n$  and  $u_{ji,r}^n$ ,  $r = 1, \dots, R$  are high-order representations of  $u$  on both sides of edge  $e_{ij}$  and  $\xi_r$  denote the quadrature weights for the numerical integration. In practice,  $u_{ij,r}^n$  and  $u_{ji,r}^n$  are two approximations of  $u(q_{ij}^r, t^n)$  at quadrature points  $q_{ij}^r \in e_{ij}$ ,  $r = 1, \dots, R$  (see figure 1).

For the sake of simplicity, let us write the scheme under the compact form

$$u_h^{n+1} = u_h^n + \Delta t \mathcal{H}^R(u_h^n), \quad (10)$$

with  $u_h^n = \sum_{i \in \mathcal{E}_{el}} u_i^n \mathbb{1}_{K_i}$  the constant piecewise approximation of function  $u$  and operator  $\mathcal{H}^R$  being defined as

$$\mathcal{H}^R(u_h^n) := - \sum_{j \in \mathcal{L}(i)} \frac{|e_{ij}|}{|K_i|} \sum_{r=1}^R \xi_r G(u_{ij,r}^n, u_{ji,r}^n, \mathbf{n}_{ij}). \quad (11)$$

**Remark 1** *Note that relation (10) can be rewritten as a convex combination of the first-order scheme (8) since weights  $\xi_r$  are positive with unit sum*

$$\begin{aligned} u_i^n - \Delta t \sum_{j \in \mathcal{L}(i)} \frac{|e_{ij}|}{|K_i|} \sum_{r=1}^R \xi_r G(u_{ij,r}^n, u_{ji,r}^n, \mathbf{n}_{ij}) = \\ \sum_{r=1}^R \xi_r \left( u_i^n - \Delta t \sum_{j \in \mathcal{L}(i)} \frac{|e_{ij}|}{|K_i|} G(u_{ij,r}^n, u_{ji,r}^n, \mathbf{n}_{ij}) \right). \end{aligned}$$

*From a practice point of view, the high-order scheme consists in applying  $R$  times the first-order scheme. Implementation effort to produce the high-order approximation is very straightforward.  $\square$*

To provide a high-order method in time, we use the third-order TVD Runge-Kutta method which corresponds to a convex combination of three explicit steps

$$u_h^{(1)} = u_h^n + \Delta t \mathcal{H}^R(u_h^n), \quad (12a)$$

$$u_h^{(2)} = u_h^{(1)} + \Delta t \mathcal{H}^R(u_h^{(1)}), \quad (12b)$$

$$u_h^{(3)} = \left( \frac{3u_h^n + u_h^{(2)}}{4} \right) + \Delta t \mathcal{H}^R \left( \frac{3u_h^n + u_h^{(2)}}{4} \right), \quad (12c)$$

$$u_h^{n+1} = \frac{u_h^n + 2u_h^{(3)}}{3}. \quad (12d)$$

The main challenge is to build the approximations  $u_{ij,r}^n$  and  $u_{ji,r}^n$  on both sides of edge  $e_{ij}$  with  $r = 1, \dots, R$  to be plugged into relations (11) and (12). Polynomial reconstructions provide high-order approximation but unphysical



oscillations arises in the vicinity of discontinuities. Indeed, the exact solution of an autonomous scalar conservation law (1) satisfies a local Maximum Principle and we intend to build the reconstructions such that this stability property is fulfilled at the numerical level (see [8] and references herein). To this end, we state the following definition.

**Definition 2** *A numerical scheme (10) satisfies the Discrete Maximum Principle (DMP) if for any cell index  $i \in \mathcal{E}_{el}$  one has*

$$\min_{j \in \bar{\nu}(i)} (u_i^n, u_j^n) \leq u_i^{n+1} \leq \max_{j \in \bar{\nu}(i)} (u_i^n, u_j^n). \quad (13)$$

### 3 A short review on MUSCL methods

All  $L^\infty$  stable high-order schemes are based on a piecewise linear reconstruction equipped with a limiting procedure. The polynomial reconstruction will provide the accuracy while the limitation algorithm will ensure the physical relevance of the numerical approximation. We briefly present the piecewise linear reconstruction step and recall a limitation procedure used in the popular MUSCL technique [39,4,21,3].

#### 3.1 Unlimited linear reconstruction

Let  $(u_i)_{i \in \mathcal{E}_{el}}$  be a set of cell centered mean values given on cells  $K_i$ ,  $i \in \mathcal{E}_{el}$ . For a generic cell  $K$ , we reconstruct a polynomial function  $\tilde{u}(\mathbf{x})$  of degree  $d = 1$  using the mean values on elements  $K_j$ ,  $j \in \nu$  where  $\nu$  is an index set of neighbouring cells.

**Criterion 3** *The polynomial reconstruction must fulfill the following criteria*

- (1)  $\left\langle \tilde{u}(\mathbf{x}) \right\rangle_K = \bar{u}$  where  $\bar{u}$  is the mean value approximation of  $u$  on  $K$ .
- (2) *The polynomial coefficients are determined as the ones that minimize the functional*

$$E(\tilde{u}) = \sum_{j \in \nu} \left( u_j - \left\langle \tilde{u}(\mathbf{x}) \right\rangle_{K_j} \right)^2. \quad (14)$$

The polynomial  $\tilde{u}$  writes

$$\tilde{u}(\mathbf{x}) = \bar{u} + (G \cdot \mathbf{x} - \bar{G}), \quad (15)$$

where  $\bar{G} = \left\langle G \cdot \mathbf{x} \right\rangle_K$  and  $G = (G_1, G_2)$  is a constant approximation of  $\nabla u(\mathbf{x})$  on  $K$ . Note that the reconstruction satisfies the first condition of criterion 3 and classical techniques like least square methods are used to determine vector  $G$  that minimizes the functional  $E$  in equation (14). Notice that if  $u$  is a linear function on the neighbourhood of the current cell then  $\tilde{u} \equiv u$ . Such a property justifies the denomination of second-order reconstruction.

### 3.2 Gradient limitation

As we mentioned above, a finite volume scheme only based on the local polynomial reconstruction without limiting procedure produces spurious oscillations. Initiated by the pioneer work of Van Leer [39], the MUSCL technique deals with a local linear reconstruction like (15) where the gradient  $G$  on each cell  $K$  is reduced by a limiter coefficient  $\phi \in [0, 1]$  such that the reconstructed values satisfy the Discrete Maximum Principle [4,21,3]

$$\tilde{u}_{lim}(\mathbf{x}) = \bar{u} + \phi \left( G \cdot \mathbf{x} - \bar{G} \right). \quad (16)$$

As an example, we hereafter detail the MLP method proposed in [27] we shall compare with our new MOOD method. Other classical limiters are also used (see for exemple [4,21,3]).

The MLP limiter proposed in [27] applies the following procedure.

- Construction of an unlimited slope  $G$  using the neighbour cells  $K_j$ ,  $j \in \bar{\nu}$ .
- Evaluation of the unlimited reconstruction (15) at the vertices  $P_m$  of  $K$ :  
 $u_m = \tilde{u}(P_m)$ ,  $m \in \lambda$ .
- Evaluation of the bounds for each node  $P_m$

$$\delta u_m^{\max} = \max_{j, K_j \ni P_m} (u_j - \bar{u}), \quad \delta u_m^{\min} = \min_{j, K_j \ni P_m} (u_j - \bar{u}).$$

- Evaluation of the vertex based limiter  $\phi_m$

$$\phi_m = \begin{cases} \min \left( 1, \frac{\delta u_m^{\max}}{u_m - \bar{u}} \right) & \text{if } u_m - \bar{u} > 0, \\ \min \left( 1, \frac{\delta u_m^{\min}}{u_m - \bar{u}} \right) & \text{if } u_m - \bar{u} < 0, \\ 1 & \text{if } u_m - \bar{u} = 0. \end{cases}$$

- Cell-centered limiter  $\phi = \min_{m \in \lambda} \phi_m$ .

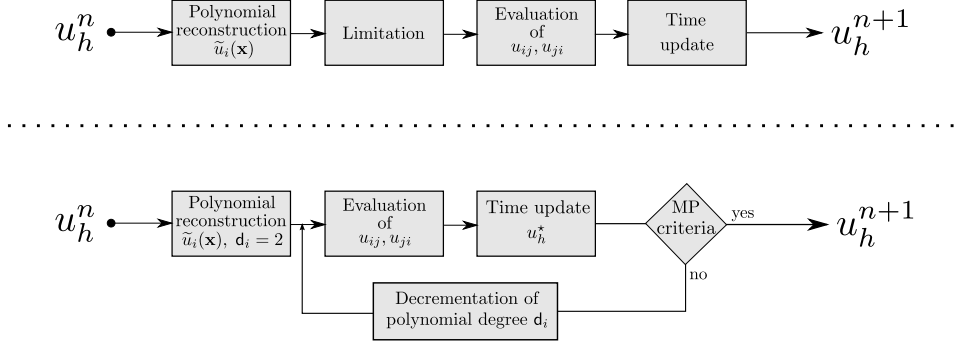


Fig. 2. Classical high-order methods idea (top) and MOOD idea (bottom).

The MLP technique provides a second-order finite volume scheme which satisfies the Discrete Maximum Principle under the CFL condition.

**Remark 4** *Although there exists a large literature about piecewise linear limitation, the extension of MUSCL type method to piecewise quadratic or even higher degree polynomial in a multi-dimensional context is not yet achieved. An efficient limitation process is still an under-investigation field of research.  $\square$*

#### 4 The Multi-dimensional Optimal Order Detection method (MOOD)

Classical high-order methods are based on a *a priori* limitation of the reconstructed values which are plugged into a one time step generic finite volume scheme to update the mean values (see figure 2 top). Unlike the existing methods, the MOOD technique proceeds in a different way since we introduce an *a posteriori* limitation. An unlimited polynomial reconstruction is carried out to build a predicted update mean value. Then the *a posteriori* limitation consists in reducing the polynomial degree and recomputing the predicted solution  $u_h^*$  until the DMP property (13) is achieved.

To this end, a prescribed maximum degree  $d_{\max}$  is introduced and used to perform an initial polynomial reconstruction on each cell. Through an iterative decremental procedure, we determine the optimal degree  $d_i \leq d_{\max}$  such that the updated mean values fulfill the DMP property (see figure 2 bottom).

In the following we focus on the quadratic polynomial case  $d_{\max} = 2$  and present the piecewise quadratic polynomial reconstruction of [26] based on a minimization technique. The MOOD method is then detailed and we prove that the numerical approximations satisfy the DMP property.

#### 4.1 Quadratic polynomial reconstruction

Using the same framework as in section 3.1, the quadratic polynomial reconstruction writes

$$\tilde{u}(\mathbf{x}) = \bar{u} + (G \cdot \mathbf{x} - \bar{G}) + \frac{1}{2} \left( \mathbf{x}^t H \mathbf{x} - \bar{H} \right), \quad (17)$$

with

$$\bar{H} = \left\langle \mathbf{x}^t H \mathbf{x} \right\rangle_K, \quad H = \begin{bmatrix} H_{11} & H_{12} \\ H_{12} & H_{22} \end{bmatrix},$$

where matrix  $H$  is an approximation of the Hessian matrix  $\nabla^2 u$  on  $K$ . Note that by construction, the mean value of  $\tilde{u}$  on  $K$  is still equal to  $\bar{u}$ .

A minimization technique is used to compute  $G$  and  $H$ . To this end, for a cell  $K_j$ , let us define the integral

$$\mathbf{x}_{K_j}^{\{\alpha, \beta\}} = \left\langle x^\alpha y^\beta \right\rangle_{K_j} - \left\langle x^\alpha y^\beta \right\rangle_K.$$

Algebraic manipulations yield the following expression for  $\left\langle \tilde{u}(\mathbf{x}) \right\rangle_{K_j}$

$$\left\langle \tilde{u}(\mathbf{x}) \right\rangle_{K_j} = \bar{u} + \left( G_1 \mathbf{x}_{K_j}^{\{1,0\}} + G_2 \mathbf{x}_{K_j}^{\{0,1\}} \right) + \frac{1}{2} \left( H_{11} \mathbf{x}_{K_j}^{\{2,0\}} + 2H_{12} \mathbf{x}_{K_j}^{\{1,1\}} + H_{22} \mathbf{x}_{K_j}^{\{0,2\}} \right). \quad (18)$$

This expression is further derived for any cell  $K_j$  such that  $j \in \nu$  to form an over-determined linear system of the form  $A\Lambda = B$  with

$$A = \begin{pmatrix} \mathbf{x}_{K_1}^{\{1,0\}} & \mathbf{x}_{K_1}^{\{0,1\}} & \mathbf{x}_{K_1}^{\{2,0\}} & \mathbf{x}_{K_1}^{\{1,1\}} & \mathbf{x}_{K_1}^{\{0,2\}} \\ \mathbf{x}_{K_2}^{\{1,0\}} & \mathbf{x}_{K_2}^{\{0,1\}} & \mathbf{x}_{K_2}^{\{2,0\}} & \mathbf{x}_{K_2}^{\{1,1\}} & \mathbf{x}_{K_2}^{\{0,2\}} \\ \vdots & \vdots & \vdots & \vdots & \vdots \\ \mathbf{x}_{K_N}^{\{1,0\}} & \mathbf{x}_{K_N}^{\{0,1\}} & \mathbf{x}_{K_N}^{\{2,0\}} & \mathbf{x}_{K_N}^{\{1,1\}} & \mathbf{x}_{K_N}^{\{0,2\}} \end{pmatrix}, \quad \Lambda = \begin{pmatrix} G_1 \\ G_2 \\ \frac{1}{2}H_{11} \\ H_{12} \\ \frac{1}{2}H_{22} \end{pmatrix}, \quad B = \begin{pmatrix} u_1 - \bar{u} \\ u_2 - \bar{u} \\ \vdots \\ u_N - \bar{u} \end{pmatrix}, \quad (19)$$

with  $N = \#\nu$ .

This system is solved using the Householder transformation computing  $A = QR$  with  $Q \in \mathcal{M}_{N \times N}(\mathbb{R})$  an orthogonal matrix and  $R \in \mathcal{M}_{N \times 5}(\mathbb{R})$  an upper-triangular matrix. Finally back-substitution of  $R\Lambda = Q^t B$  defines  $\tilde{u}$  (see [26]).

**Remark 5** *A left preconditioner matrix can be applied to reduce the system sensitivity. For example, in [26], the authors use a diagonal matrix whose coefficients  $\omega_{jj} = \|c_j - c\|^{-2}$  ( $j = 1, \dots, N$ ) correspond to geometrical weights in order to promote closest information.  $\square$*

	EPD <sub>0</sub> strategy	EPD <sub>1</sub> strategy	EPD <sub>2</sub> strategy
<b>EdgePD</b> $d_{ij}$	$d_i$	$\min(d_i, d_j)$	$\min_{j \in \mathcal{V}(i)} (d_i, d_j)$

Table 1

Evaluation of the EdgePD  $d_{ij}$  using the CellPD of the neighbour elements.

#### 4.2 Description of the MOOD method

We now detail the MOOD technique considering the simple case where an explicit time discretisation is employed. Moreover, without loss of generality, we present the method using only one quadrature point,  $R = 1$ , and skip the subscript  $r$  denoting  $u_{ij}$  in place of  $u_{ij,r}$ . Extension to several quadrature points, *i.e.*  $R > 1$ , is straightforward.

Assume that we have a given sequence  $u_h^n = (u_i^n)_i$ ,  $i \in \mathcal{E}_{el}$  of mean value approximations at time  $t^n$ , the goal is to build a new sequence  $u_h^{n+1} = (u_i^{n+1})_i$  at time  $t^{n+1} = t^n + \Delta t$ . To this end, we define the following fundamental notions.

- $d_i$  is the Cell Polynomial Degree (CellPD) which represents the degree of the polynomial reconstruction on cell  $K_i$ ;
- $d_{ij}$  and  $d_{ji}$  are the Edge Polynomial Degrees (EdgePD) which correspond to the effective degrees we use to respectively build  $u_{ij}$  and  $u_{ji}$  on both sides of edge  $e_{ij}$ .

The MOOD method consists in the following iterative procedure.

1. **CellPD initialisation.** Each CellPD is initialized with  $d_{max}$ .
2. **EdgePD evaluation.** Each EdgePD is set up as a function of the neighbours CellPD thanks to one of the methods proposed in table 1.
3. **Quadrature points evaluation.** Each  $u_{ij}$  is evaluated with the polynomial reconstruction of degree  $d_{ij}$  at the quadrature point.
4. **Mean values update.** The updated values  $u_h^*$  are computed using the finite volume scheme (10).
5. **DMP test.** The DMP criterion is checked on each cell, that is

$$\min_{j \in \mathcal{V}(i)} (u_i^n, u_j^n) \leq u_i^* \leq \max_{j \in \mathcal{V}(i)} (u_i^n, u_j^n). \quad (20)$$

If  $u_i^*$  does not satisfy (20) the CellPD is decremented, *i.e.*  $d_i := \max(0, d_i - 1)$ .

6. **Stopping criterion.** If all cells satisfy the DMP property, the iterative procedure stops with  $u_h^{n+1} = u_h^*$  else go to Step 2.

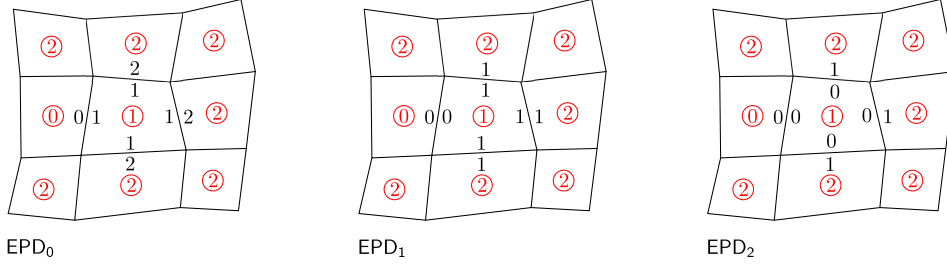


Fig. 3. Value of EdgePD according to the EPD strategy. The CellPD are in red and the EdgePD are in black. Every omitted CellPD are equal to 2.

**Remark 6** *From a practice point of view, we do not have to recompute the polynomials if  $d_{ij}$  is modified in step 2 but we perform a simple truncation of the initial polynomial of degree  $d_{max}$ .  $\square$*

**Remark 7** *Only cells where CellPD has been decremented and their neighbours in a compact stencil have to be updated. For instance, if  $d_i$  is decremented, we only have to update the  $K_i$  cell and all the  $K_j$ ,  $j \in \mathcal{V}(i)$ .  $\square$*

To conclude the section, we give in figure 3 an example of the three strategies of EdgePD calculation proposed in table 1. The simplest strategy named  $EPD_0$  consists in setting  $d_{ij} = d_i$  and  $d_{ji} = d_j$  while  $EPD_1$  chooses the minimal value between  $d_i$  and  $d_j$  for both  $d_{ij}$  and  $d_{ji}$ . At last, the smallest CellPD of all the neighbour cells is taken in the  $EPD_2$  strategy.

#### 4.3 Convergence of the MOOD method

We first recall the classical stability result (see for example [9] and the references herein).

**Proposition 8** *Let us consider the generic first-order finite volume scheme (7) with reflective boundary conditions. If the numerical flux is consistent and monotone, then the DMP property given by definition 2 is satisfied.*

It implies that if  $u_{ij} = u_i$  and  $u_{ji} = u_j$  for all  $j \in \mathcal{V}(i)$  then relation (13) holds. To prove that the iterative MOOD method provides a solution which satisfies the DMP, we introduce the following definition.

**Definition 9** *An EPD strategy is said upper-limiting (with respect to the CellPD) if for any  $K_i$*

$$d_i = \bar{d} \implies d_{ij} \leq \bar{d} \quad \text{and} \quad d_{ji} \leq \bar{d}. \quad (21)$$

**Remark 10** *Note that  $EPD_1$  and  $EPD_2$  are upper-limiting strategies whereas  $EPD_0$  strategy does not satisfy condition (21).  $\square$*

We then have the following theorem.

**Theorem 11** *Let us consider the generic high-order finite volume scheme with reflective boundary conditions and assume that the numerical flux is consistent and monotone. If the EPD strategy is upper-limiting then the MOOD method provides an updated solution  $u_h^{n+1}$  which satisfies the DMP property with a finite number of iterations.*

PROOF. Let  $\mathbf{d}_i$  be the CellPD of cell  $K_i$ . If  $\mathbf{d}_i = 0$ , then equation (21) implies that  $\mathbf{d}_{ij} = \mathbf{d}_{ji} = 0$ , hence  $u_{ij}^n = u_i^n$  and  $u_{ji}^n = u_j^n$ , for all  $j \in \underline{\nu}(i)$ . We recover the first-order scheme (8) and proposition 8 yields that  $u_i^{n+1}$  satisfies the DMP property (13). Otherwise, if  $\mathbf{d}_i > 0$  then two situations arise. Either the Maximum principle is satisfied and we do not modify  $\mathbf{d}_i$  or we decrement  $\mathbf{d}_i$ . Consequently if the maximum principle is not satisfied for all the cells, then there is at least one cell having its CellPD positive which has to be decremented. Since we can not decrement more than  $d_{\max} \times \#(\mathcal{E}_{el})$  times, the iterative procedure stops after a finite number of iterations and the solution satisfies the DMP property.  $\square$

**Remark 12** *To carry out a third-order Runge-Kutta time discretisation (12) which provides a solution satisfying the DMP property, one has to performe the MOOD procedure for each explicit substep since (12) rewrites as a convex combination.*  $\square$

## 5 Extension to hyperbolic system

We develop an extension of the MOOD method to hyperbolic system. For the sake of simplicity, we only deal with the Euler system

$$\partial_t \begin{pmatrix} \rho \\ \rho u_1 \\ \rho u_2 \\ E \end{pmatrix} + \partial_{x_1} \begin{pmatrix} \rho u_1 \\ \rho u_1^2 + p \\ \rho u_1 u_2 \\ u_1(E + p) \end{pmatrix} + \partial_{x_2} \begin{pmatrix} \rho u_2 \\ \rho u_1 u_2 \\ \rho u_2^2 + p \\ u_2(E + p) \end{pmatrix} = 0, \quad (22)$$

where  $\rho$ ,  $\mathbf{V} = (u_1, u_2)$  and  $p$  are the density, velocity and pressure respectively while the total energy per unit volume  $E$  is given by

$$E = \rho \left( \frac{1}{2} \mathbf{V}^2 + e \right), \quad \mathbf{V}^2 = u_1^2 + u_2^2,$$

where  $e$  is the specific internal energy. For an ideal gas, this system is closed by the equation of state

$$e = \frac{p}{\rho(\gamma - 1)},$$

with  $\gamma$  the ratio of specific heats.

Despite that the physical variables do not have to respect the maximum principle, classical methods such as the MUSCL technique use a limiting procedure derived from the scalar case to keep the numerical solution from producing spurious oscillations. A popular choice consists in reconstructing and limiting the density, the velocity components and the pressure variables but other limitations can be carried out: the internal energy, the specific volume or the characteristic variables for instance. We propose here several strategies in the MOOD framework to both perform an accurate reconstruction in domains where the solution is regular enough, still preventing the oscillations from appearing close to the discontinuities.

The keypoints of the MOOD method is the **CellPD** decrementing procedure and the **EdgePD** strategy. As in the scalar case, we first build the local polynomial reconstruction of maximal degree  $d_{\max}$  for the density, the velocity components and the pressure. A natural idea would be to apply the MOOD method to the four variables independently. We have carried out numerical simulations and obtained physically admissible solution but we observe an excessive diffusion.

To reduce the diffusion amount, we propose the new strategy where the DMP test (step 5 of section 4.2) is substituted with the following stages.

- **Density DMP test.** The DMP criterion is checked on the density that is

$$\min_{j \in \mathcal{V}(i)} (\rho_i^n, \rho_j^n) \leq \rho_i^* \leq \max_{j \in \mathcal{V}(i)} (\rho_i^n, \rho_j^n). \quad (23)$$

If  $\rho_i^*$  does not satisfy (23) the **CellPD** is decremented:  $\mathbf{d}_i := \max(0, \mathbf{d}_i - 1)$ .

- **Pressure positivity preserving test.** The pressure positivity is checked and if  $p_i^* \leq 0$  and  $\mathbf{d}_i$  has not been altered by the density DMP test then the **CellPD** is decremented:  $\mathbf{d}_i := \max(0, \mathbf{d}_i - 1)$ .

Numerical experiments with this strategy give good results with low diffusion and we shall adopt it in the remaining of the paper.



## 6 Numerical results: the scalar case

We first consider a scalar problem where the scalar quantity  $u$  is convected with velocity  $V(\mathbf{x}, t)$ . Several series of tests are proposed and comparisons with the classical MUSCL method are drawn.

Let  $\Omega$  be the unit square  $[0, 1] \times [0, 1]$ . We consider the linear convection problem

$$\partial_t u + \nabla \cdot (Vu) = 0, \quad (24a)$$

$$u(., 0) = u^0, \quad (24b)$$

where  $V(\mathbf{x}, t)$  is a given continuous function on  $\Omega \times [0, T]$  and  $u^0$  the initial function we shall characterize in the following. Moreover, periodic boundary conditions are prescribed on  $\partial\Omega$ . Comparisons are carried out between the simple first-order finite volume method (FV), the MUSCL method proposed in [27] (MLP) and the MOOD method with  $d_{\max} = 1$  (MOOD-P1) and  $d_{\max} = 2$  (MOOD-P2).

### 6.1 Numerical flux

The monotone upwind numerical flux writes

$$G(u_i^n, u_j^n, \mathbf{n}_{ij}) = [V(\mathbf{x}, t^n) \cdot \mathbf{n}_{ij}]^+ u_i^n + [V(\mathbf{x}, t^n) \cdot \mathbf{n}_{ij}]^- u_j^n,$$

where the velocity is evaluated at the quadrature point  $\mathbf{x}$  and the positive and negative parts are respectively defined by

$$[\alpha]^+ = \max(0, \alpha) \quad \text{and} \quad [\alpha]^- = \min(0, \alpha).$$

Two Gauss points are used on each edge to provide a third-order accurate numerical integration. On the other hand, time integration is performed with a forward Euler scheme for the FV method whereas the RK3-TVD method given by system (12) is employed for the MLP and MOOD methods.

**Remark 13** *We use the most obvious implementation of MOOD where we simply apply the procedure detailed in section 4.2 to each substep of system (12). Indeed, the CellPD are reinitialized to  $d_{\max}$  at the beginning of each substep.*

## 6.2 Test descriptions

Three classical numerical experiments are carried out to demonstrate the ability of the method to provide effective third-order accuracy and to handle discontinuities with a very low numerical diffusion.  $L^1$  and  $L^\infty$  errors are evaluated with

$$err_1 = \sum_{i \in \mathcal{E}_{el}} |u_i^N - u_i^0| |K_i| \quad \text{and} \quad err_\infty = \max_{i \in \mathcal{E}_{el}} |u_i^N - u_i^0|,$$

where  $(u_i^0)_i$  and  $(u_i^N)_i$  are respectively the cell mean values at initial time  $t = 0$  and final time  $t = t_f = N\Delta t$ .

*Double Sine Translation (DST):*

We consider a constant velocity  $V = (2, 1)$  and the initial condition is the  $C^\infty$  initial condition

$$u^0(x_1, x_2) = \sin(2\pi x_1) \sin(2\pi x_2).$$

The final time  $t_f = 2.0$ .

*SQuare Translation(SQT):*

We consider a constant velocity  $V = (2, 1)$  and the initial condition is the square wave defined by

$$u^0(x_1, x_2) = \begin{cases} 1 & \text{if } |x_1 - 0.4| < 0.25 \text{ and } |x_2 - 0.5| < 0.25, \\ 0 & \text{elsewhere.} \end{cases}$$

The final time  $t_f = 2.0$ .

*Solid Body Rotation(SBR):*

First introduced by R.J. Leveque in [23], this solid body rotation test uses three shapes which are a hump, a cone and a slotted cylinder. Each shape is located within a circle of radius  $r^0 = 0.15$  and centered at  $(x_1^0, y_2^0)$

Hump centered at  $(x_1^0, x_2^0) = (0.25, 0.5)$

$$u^0(x_1, x_2) = \frac{1}{4}(1 + \cos(\pi \min(r(x_1, x_2), 1))).$$

Cone centered at  $(x_1^0, x_2^0) = (0.5, 0.25)$

$$u^0(x_1, x_2) = 1 - r(x_1, x_2).$$

Table 2

$L^1$  and  $L^\infty$  errors and convergence rates for DST problem with the MOOD-P2 method: EPD<sub>1</sub> (left) and EPD<sub>2</sub> (right).

Nb of Cells	EPD <sub>1</sub>				EPD <sub>2</sub>			
	$err_1$		$err_\infty$		$err_1$		$err_\infty$	
20x20	9.469E-02	—	3.960E-01	—	1.104E-01	—	4.506E-01	—
40x40	1.113E-02	3.09	1.333E-01	1.57	1.382E-02	3.00	1.566E-01	1.52
80x80	1.768E-03	2.65	4.164E-02	1.68	2.309E-03	2.58	5.196E-02	1.59
160x160	2.481E-04	2.83	1.304E-02	1.68	3.262E-04	2.82	1.698E-02	1.61

Slotted cylinder centered at  $(x_1^0, x_2^0) = (0.5, 0.75)$

$$u^0(x_1, x_2) = \begin{cases} 1 & \text{if } |x_1 - 0.5| < 0.25, \text{ or } x_2 > 0.85 \\ 0 & \text{elsewhere,} \end{cases}$$

where  $r(x_1, x_2) = \frac{1}{r_0} \sqrt{(x_1 - x_1^0)^2 + (x_2 - x_2^0)^2}$ . To perform the rotation, we use the velocity  $V = (-x_2 + 0.5, x_1 - 0.5)$  and the final time  $t_f = 2\pi$  corresponds to one full rotation.

### 6.3 Numerical results

#### 6.3.1 Comparison between EPD<sub>1</sub> and EPD<sub>2</sub> strategies

We consider the DST approximations on uniform meshes from  $20 \times 20$  to  $160 \times 160$  cells and compare the  $L^1$  and  $L^\infty$  errors and convergence rates displayed in table 2 using EPD<sub>1</sub> and EPD<sub>2</sub> strategies with the MOOD -P2 method. We obtain in table 2 an almost effective third-order convergence in  $L^1$  norm and a 1.6 convergence rate in  $L^\infty$  norm for the two strategies. We observe in this case that the  $L^1$  and  $L^\infty$  errors for EPD<sub>1</sub> are slightly less important than the EPD<sub>2</sub> and the convergence orders seem to indicate that the EPD<sub>1</sub> strategy should be privileged. Moreover, from a practical point of view, the EPD<sub>1</sub> implementation is performed with a more compact stencil than the EPD<sub>2</sub> (see remark 7).

#### 6.3.2 Comparison between FV, MLP, MOOD-P1 and MOOD-P2 with EPD<sub>1</sub> strategy on uniform meshes

##### Double Sine Translation.

We report in table 3, 4 and 5 the  $L^1$  and  $L^\infty$  errors and convergence rates

Table 3

$L^1$  and  $L^\infty$  errors and convergence rates for the DST with FV and MLP methods.

Nb of Cells	FV				MLP			
	$err_1$		$err_\infty$		$err_1$		$err_\infty$	
20x20	3.924E-01	—	9.371E-01	—	1.417E-01	—	3.765E-01	—
40x40	3.480E-01	0.17	8.375E-01	0.16	3.038E-02	2.22	1.121E-01	1.75
80x80	2.663E-01	0.39	6.241E-01	0.42	6.904E-03	2.14	3.534E-02	1.67
160x160	1.734E-01	0.62	3.964E-01	0.65	1.693E-03	2.03	1.167E-02	1.60

Table 4

$L^1$  and  $L^\infty$  errors and convergence rates for the DST with MOOD-P1 and MOOD-P2 methods.

Nb of Cells	MOOD-P1				MOOD-P2			
	$err_1$		$err_\infty$		$err_1$		$err_\infty$	
20x20	1.502E-01	—	4.876E-01	—	9.469E-02	—	3.960E-01	—
40x40	3.141E-02	2.26	1.629E-01	1.58	1.113E-02	3.09	1.333E-01	1.57
80x80	7.438E-03	2.08	5.188E-02	1.65	1.768E-03	2.65	4.164E-02	1.68
160x160	1.787E-03	2.06	1.675E-02	1.63	2.481E-04	2.83	1.304E-02	1.68

Table 5

$L^1$  and  $L^\infty$  errors and convergence orders for the DST with P1 and P2 methods.

Nb of Cells	P1				P2			
	$err_1$		$err_\infty$		$err_1$		$err_\infty$	
20x20	1.334E-01	—	3.227E-01	—	7.130E-02	—	1.729E-01	—
40x40	2.896E-02	2.20	6.593E-02	2.29	9.877E-03	2.85	2.427E-02	2.83
80x80	6.604E-03	2.13	1.408E-02	2.23	1.255E-03	2.98	3.091E-03	2.97
160x160	1.603E-03	2.04	3.310E-03	2.09	1.573E-04	3.00	3.876E-04	3.00

for FV, MLP, MOOD-P1, MOOD-P2, unlimited P1 and P2 reconstruction methods respectively. At last, we plot in figure 4 the convergence curves for the four methods as well as the convergence curves for the unlimited version.

The high-order finite volume method with the two Gauss points and the RK3 time scheme reach the optimal convergence rate for the unlimited P1 and P2 reconstructions hence the accuracy discrepancy has to be charged to the limiting procedure.

Figure 4 shows that the optimal convergence rate in  $L^1$  error for P1, MOOD-P1 and MLP methods is achieved since the curves fit very well. On the other

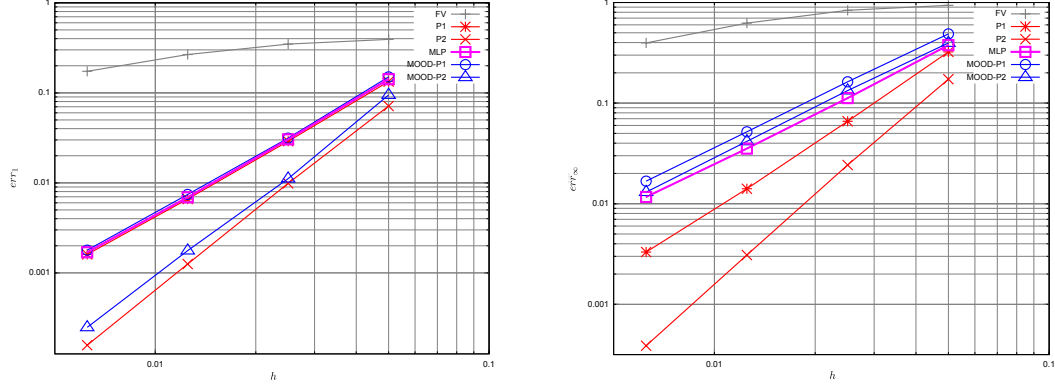


Fig. 4. Convergence curves  $err_1$ (left) and  $err_\infty$ (right).

Table 6

Min and Max for SQT with MLP, MOOD-P1 and MOOD-P2.

Nb of Cells	MLP		MOOD-P1		MOOD-P2	
	Min	Max	Min	Max	Min	Max
20x20	1.224E-03	9.392E-01	9.044E-04	8.691E-01	2.300E-04	9.187E-01
40x40	5.602E-07	9.998E-01	2.496E-07	9.964E-01	1.125E-07	9.995E-01
80x80	5.160E-08	1.000	7.520E-08	1.000	1.145E-08	1.000

hand, the P2 and MOOD-P2 curves are very close and parallel which confirm that MOOD-P2 is an effective third-order method for the  $L^1$  norm. For the  $L^\infty$  norm, none of the limited method is over the effective second-order while the unlimited P1 and P2 provide an effective second- and third-order respectively. Indeed the strict maximum principle application at extrema is responsible for the  $L^\infty$  error discrepancy and we can expect nothing more than a second-order scheme in  $L^\infty$  norm, whatever the polynomial degree is when the DMP condition is enforced.

#### *Square Translation.*

The next issue we address concerns the translation of a discontinuous shape to observe the scheme ability to preserve the discontinuity. Table 6 gives the minimum and maximum values of the solution using the three reconstruction methods where we check that the maximum principle is respected for all the methods. Notice that the CFL condition is set in order to satisfy the DMP property for each time step.

In figure 5, we display the  $L^1$  errors for the three methods. An effective 0.70 convergence rate is achieved by the three reconstruction but the MOOD-P2 provides the best accuracy. We print in the left panels of figure 6 elevations of the solutions while the right panels show 10 isolines top view uniformly ranged from 0 to 1. MOOD-P1 and MLP methods provide very similar results

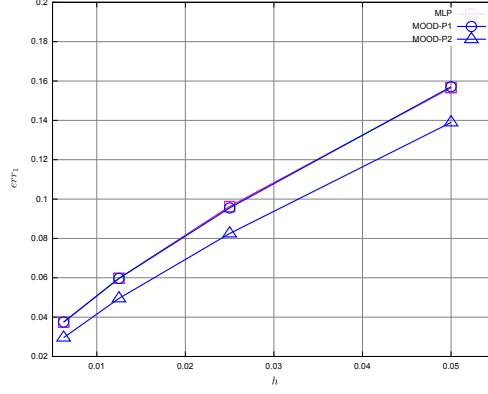


Fig. 5. Convergence curves in  $L^1$  norm with the MLP, MOOD-P1 and MOOD-P2 for SQT problem.

whereas the third-order MOOD-P2 method gives a solution with sharper discontinuities. We observe that that MOOD-P2 method succeeds in preserving the shape symmetry whereas the MLP and MOOD-P1 methods do not.

#### *Solid Body Rotation.*

The last test of this subsection concerns the solid body rotation where three shapes are clockwise rotated. We employ a  $140 \times 140$  uniform mesh of squared element in order to compare our results with  $100 \times 100 \times 2$  triangular mesh in reference [27].

We display in the left panels of figure 7 a three-dimensional elevation while we print on the right panels top views of the ten uniformly distributed isolines from 0 to 1. we can measure the scheme accuracy by counting the number of isolines outside of the slot since the exact solution isolines would fit the slot shape. The smaller number of isolines outside of the slot is, the better the scheme is. With the MLP reconstruction, we observe three isolines outside while we have only two with the MOOD-P1. At last, the outstanding result is that we have just one isoline outside of the slot with the MOOD-P2 method which proves the great ability of the technique to handle and preserve discontinuities.

#### *6.3.3 Comparison between FV, MLP, MOOD-P1 and MOOD-P2 with EPD<sub>1</sub> strategy on distorted meshes*

Approximation accuracy is reduced when one employs meshes with large deformation, *i.e.* the elements are no longer rectangular but quadrilateral with large aspect ratio. The present subsection investigates the MOOD method sensitivity with mesh distortion.

To obtain the distorted mesh, we proceed in two stages. First the following

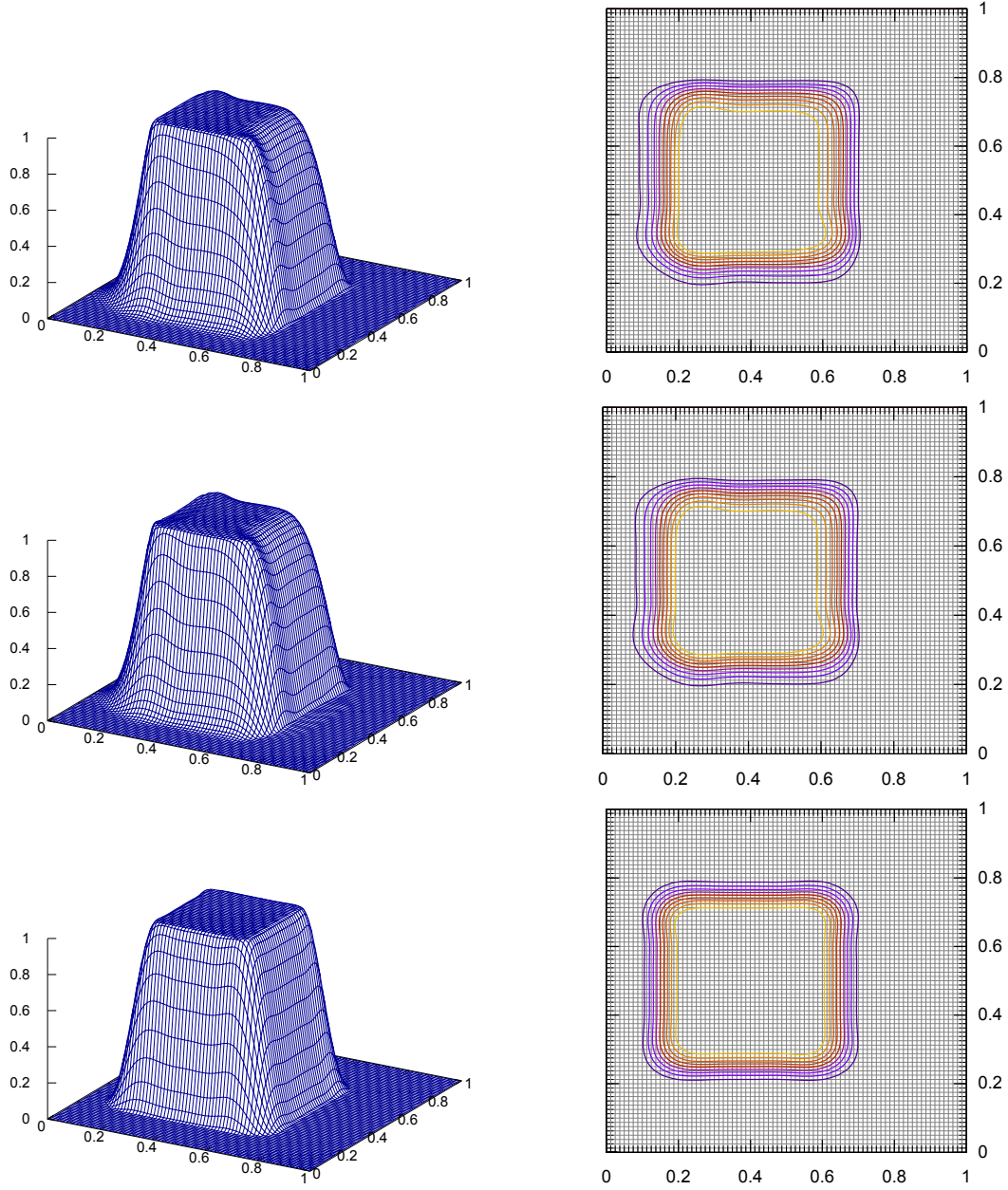


Fig. 6. Results on 80x80 of SQT — Top: MLP method — Middle: MOOD-P1 method — Bottom: MOOD-P2 method.

transformation is applied to the uniform mesh

$$x_1 \rightarrow \begin{cases} x_1(10x_1^2 + 5x_1 + 1), & \text{if } x_1 \leq 0.5, \\ (x_1 - 1)(10(x_1 - 1)^2 + 5(x_1 - 1)) + 1, & \text{elsewhere,} \end{cases}$$

and we operate in the same way with variable  $x_2$ .  
Then we apply a second transformation



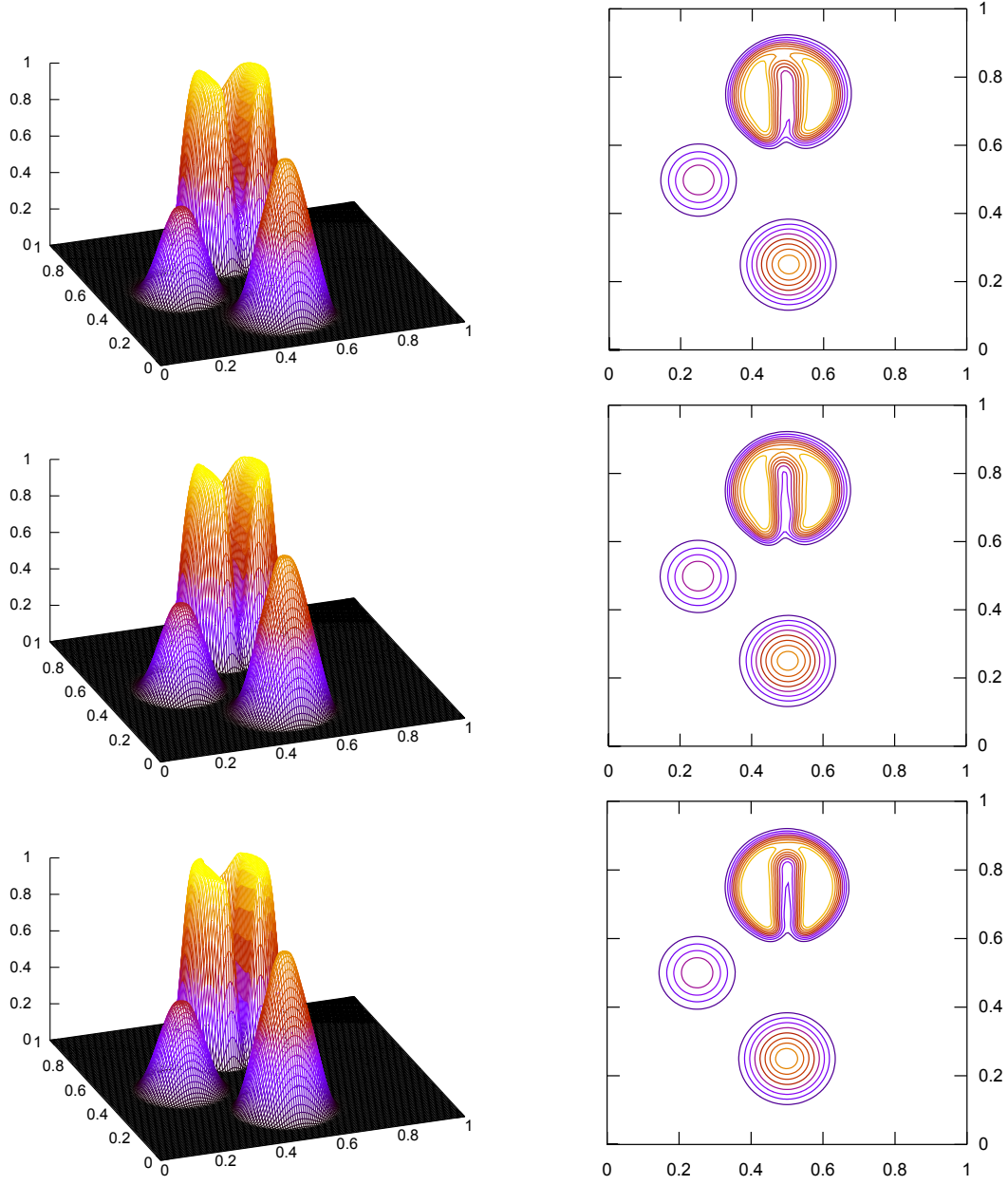


Fig. 7. Results on 140x140 of SBR. Isolines are from 0 to 1 by 0.1. Top: MLP method — Middle: MOOD-P1 method — Bottom: MOOD-P2 method.

$$\begin{aligned} x_1 &\rightarrow x_1 + 0.1|x_1 - 0.5| \cos(6\pi(x_2 - 0.5)) \sin(4\pi(x_1 - 0.5)), \\ x_2 &\rightarrow x_2 + 0.1|x_2 - 0.5| \cos(4\pi(x_1 - 0.5)) \sin(6\pi(x_2 - 0.5)). \end{aligned}$$

As an example a distorted mesh is given in figure 9. Notice that domain  $\Omega$  is shape preserved by the transformation.

Since we use periodic boundary conditions, the final time corresponds to a full revolution such that the exact solution coincides with the initial one.

*Double Sine Translation.*

We report in tables 7, 8 and 9 the  $L^1$  and  $L^\infty$  errors and convergence rates



Table 7

$L^1$  and  $L^\infty$  errors and convergence rates for the DST with FV and MLP methods.

Nb of Cells	FV				MLP			
	$err_1$		$err_\infty$		$err_1$		$err_\infty$	
20x20	4.053E-01	—	9.032E-01	—	3.907E-01	—	8.752E-01	—
40x40	4.038E-01	0.01	9.822E-01	-0.12	1.893E-01	1.05	5.306E-01	0.72
80x80	3.834E-01	0.07	9.486E-01	0.05	4.370E-02	2.11	1.806E-01	1.55
160x160	3.144E-01	0.29	7.825E-01	0.28	9.846E-03	2.15	5.889E-02	1.62

Table 8

$L^1$  and  $L^\infty$  errors and convergence rates for the DST with MOOD-P1 and MOOD-P2 methods.

Nb of Cells	MOOD-P1				MOOD-P2			
	$err_1$		$err_\infty$		$err_1$		$err_\infty$	
20x20	3.770E-01	—	8.557E-01	—	3.408E-01	—	7.897E-01	—
40x40	1.599E-01	1.24	4.541E-01	0.91	8.992E-02	1.92	3.222E-01	1.29
80x80	3.892E-02	2.04	1.314E-01	1.79	1.375E-02	2.71	9.199E-02	1.81
160x160	9.170E-03	2.09	3.374E-02	1.96	1.922E-03	2.84	2.483E-02	1.89

Table 9

$L^1$  and  $L^\infty$  errors and convergence rates for the DST with P1 and P2 methods.

Nb of Cells	P1				P2			
	$err_1$		$err_\infty$		$err_1$		$err_\infty$	
20x20	3.658E-01	—	8.312E-01	—	FAIL	—	FAIL	—
40x40	1.534E-01	1.25	3.793E-01	1.13	8.328E-02	—	2.135E-01	—
80x80	3.856E-02	1.99	9.760E-02	1.96	1.403E-02	2.57	3.582E-02	2.58
160x160	9.052E-03	2.09	2.643E-02	1.88	1.920E-03	2.87	4.917E-03	2.86

for FV, MLP, MOOD-P1, MOOD-P2, unlimited P1 and P2 reconstruction methods respectively. At last, we plot in figure 8 the convergence curves for the four methods as well as the convergence curves for the unlimited version.

We first observe in table 9 an accuracy discrepancy with the unlimited reconstructions since the errors are roughly ten times larger for the distorted mesh than for the uniform one given in table 5. Nevertheless, we obtain good effective rates of convergence both in  $L^1$  and  $L^\infty$  norm for the P1 and P2 reconstructions. Optimal second-order scheme is achieved for the P1 method and convergence rate is around 2.9 for the P2 reconstruction.

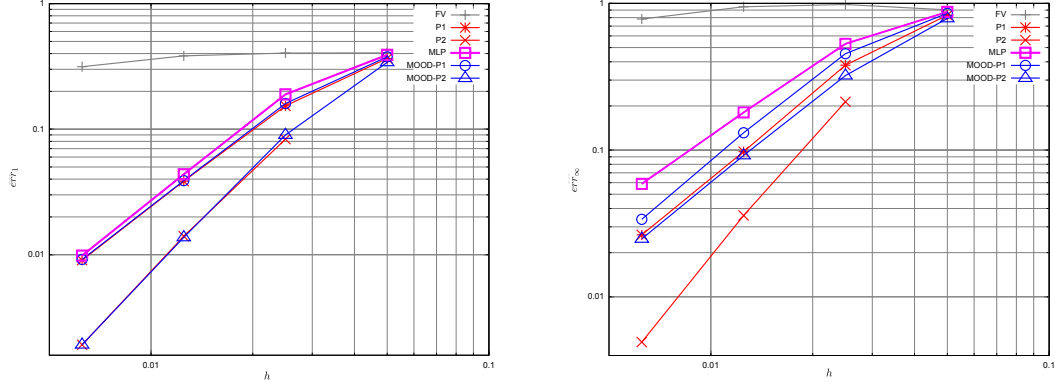


Fig. 8. Convergence curves  $err_1$ (left) and  $err_\infty$ (right).

Table 10

Min and Max for DST with MLP, MOOD-P1 and MOOD-P2.

Nb of Cells	MLP		MOOD-P1		MOOD-P2	
	Min	Max	Min	Max	Min	Max
20x20	-3.740E-02	3.479E-02	-7.168E-02	7.566E-02	-1.376E-01	1.516E-01
40x40	-4.634E-01	4.645E-01	-5.445E-01	5.458E-01	-6.738E-01	6.792E-01
80x80	-8.179E-01	8.204E-01	-8.747E-01	8.743E-01	-9.098E-01	9.079E-01
160x160	-9.433E-01	9.431E-01	-9.655E-01	9.668E-01	-9.752E-01	9.748E-01

For the  $L^1$  norm, P1, MOOD-P1 and MLP convergence curves fit well hence we get the optimal accuracy with the three methods. In the same way, the P2 and MOOD-P2 are also superimposed which means that MOOD-P2 is optimal with respect to the unlimited case. For the  $L^\infty$  norm, MLP method convergence rate is around 1.6 whereas the MOOD-P1, MOOD-P2 and P1 provide a 1.9 convergence rate. Notice that the MOOD-P2 produces more accurate results but does not reach the third-order convergence since it has to respect a strict DMP property.

Table 10 shows that the extrema are better approximated with respect to the exact solution with the MOOD methods than the MLP method, in particular when coarse meshes are employed.

#### *Square Translation.*

Table 11 gives the minimum and maximum values of the solution using the three reconstruction methods and we check that the maximum principle is respected for all the methods. The MOOD methods manage to compute a solution whose the minima are very close to the theoretical ones which suggest that the discontinuity is less diffused.

We print in the left panels of figure 9 elevations of the solutions while the right panels show 10 isolines top view uniformly ranged from 0 to 1. MOOD-P1 and

Table 11

Min and Max for SQT with MLP, MOOD-P1 and MOOD-P2.

Nb of Cells	MLP		MOOD-P1		MOOD-P2	
	Min	Max	Min	Max	Min	Max
20x20	9.185E-02	4.312E-01	2.562E-02	5.181E-01	1.089E-02	6.030E-01
40x40	5.221E-03	8.555E-01	1.759E-04	9.299E-01	1.167E-05	9.836E-01
80x80	1.493E-05	9.975E-01	2.016E-07	9.998E-01	3.467E-08	1.000

MLP methods provide very similar results whereas the third-order MOOD-P2 method gives a solution with sharper discontinuities. We observe that that MOOD-P2 method succeeds in preserving the shape symmetry whereas the MLP and MOOD-P1 methods do not.

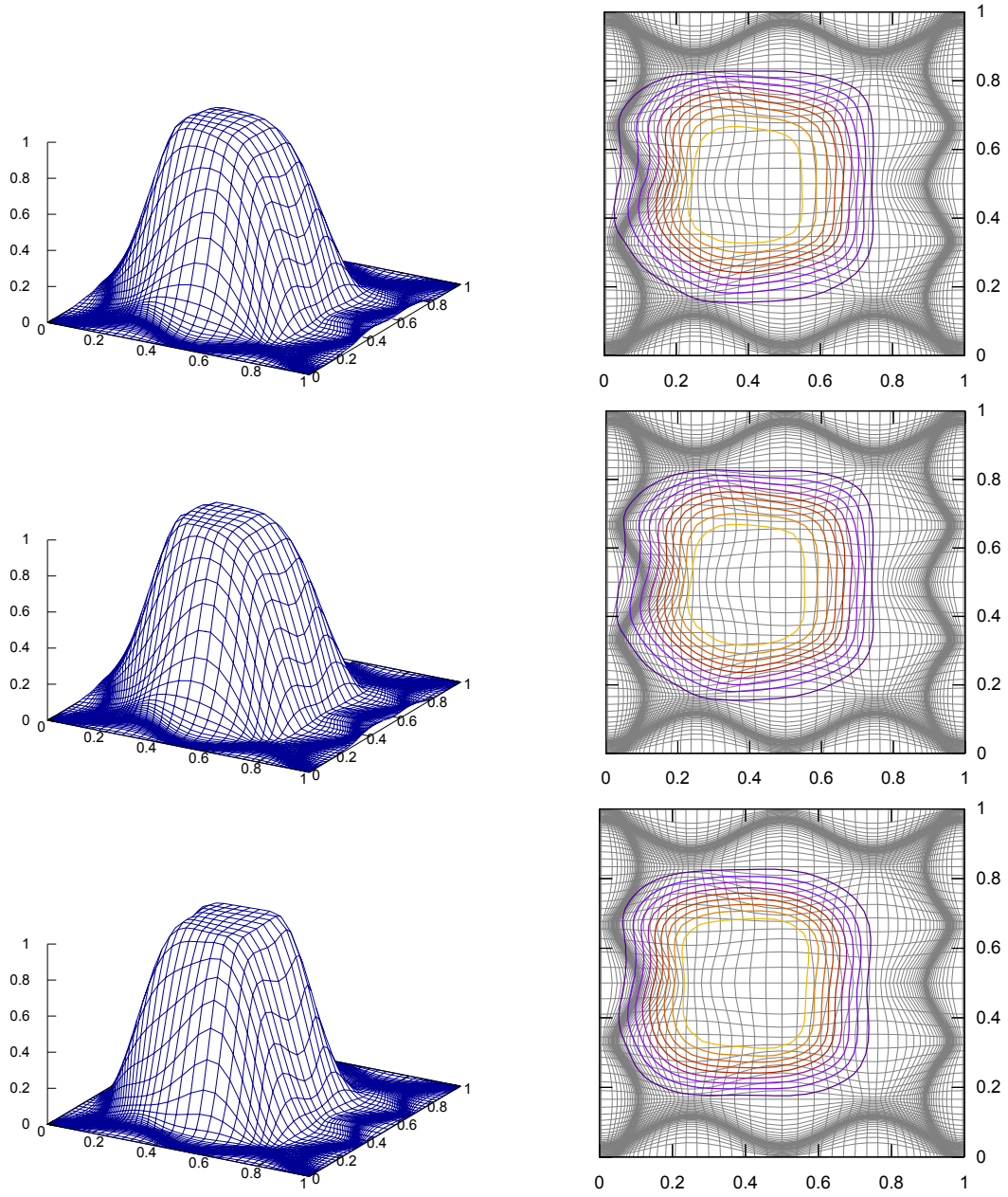


Fig. 9. Results on 80x80 of SQT — Top: MLP method — Middle: MOOD-P1 method — Bottom: MOOD-P2 method.

## 7 Numerical results: the Euler case

We now turn to the Euler equations (22) to test the MOOD method. Efficiency, accuracy and stability of the method are investigated on classical tests. In the present article, we use the HLL numerical flux detailed in [36]. To draw comparisons with the popular MUSCL method, we have implemented the MLP technique proposed in [27]. We apply the MOOD method using the detection strategy presented in section 5.

To assess the accuracy of the MOOD method, we have carried out several numerical simulations. The first test is the classical 1D Sod shock tube to test the ability of MOOD in reproducing simple waves. It is also used as a sanity check. Then we proceed with a 2D Riemann problem proposed by [34] (see also [24]). We conclude the series of tests with two classical references: The forward step problem [43,27] and the double Mach problem [43,27]. All tests are run with MOOD-P1 and MOOD-P2 on an uniform mesh. MOOD-P1 is then compared with MLP method and we visually observe the improvement when MOOD-P2 is to be used. Finally these test cases are run on deformed meshes to check the ability of MOOD to perform on non-uniform meshes.

### 7.1 Sod Shock Tube

The one dimensional Sod problem is used as a sanity check for MOOD. The computational domain is the rectangular domain  $\Omega = [0, 1] \times [0, 0.2]$ . The solution is invariant in  $y$ -direction. The interface between a left state  $(\rho_L, u_L, v_L, p_L) = (1, 0, 0, 1)$  and a right one  $(\rho_R, u_R, v_R, p_R) = (0.125, 0, 0, 0.1)$  is located at  $x = 0.5$ . Reflective boundary conditions are prescribed. The final time is  $t_f = 0.2$ .

#### Uniform mesh

The computational domain is uniformly meshed by 100 cells in the  $x$  direction and 10 cells in the  $y$  direction. We plot the pressure and the density at the final time against the exact solution using the MLP, MOOD-P1 and MOOD-P2 reconstruction in figure 10. The curves show a very good agreement between the three methods. The plateau between the contact and the shock is wavy with the MLP reconstruction while MOOD produces better constant states. However we observe an undershoot at the tail of the rarefaction with MOOD-P2 both for the density and the velocity.

#### Non-uniform mesh

The same simulation is performed on a non-uniform mesh depicted in figure 11. We plot the density and the  $x$ -velocity at the final time using the MLP, MOOD-P1 and MOOD-P2 reconstruction in figure 12. All cell values

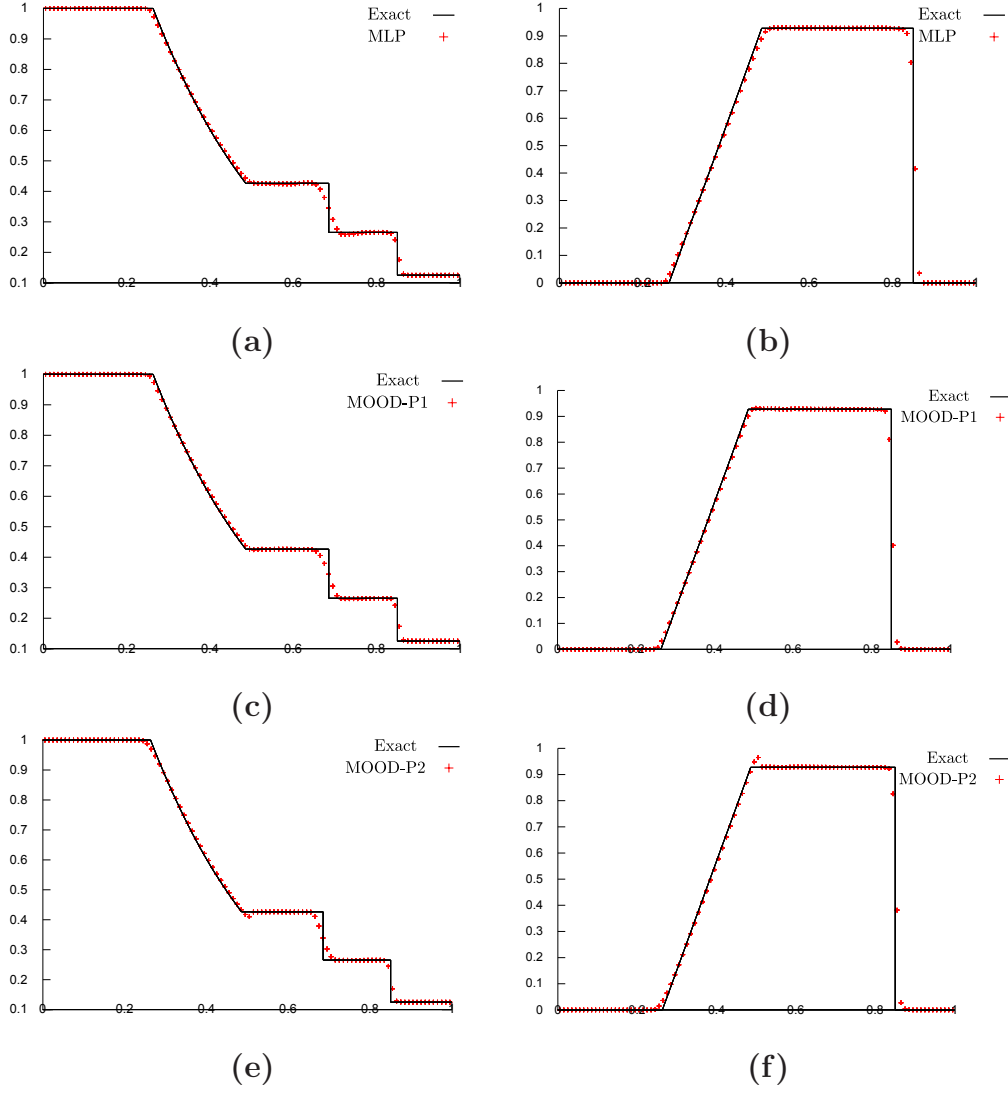


Fig. 10. Sod shock tube problem: Density and  $x$ -velocity on  $100 \times 10$  uniform mesh for (a-b): MLP — (c-d): MOOD-P1 — (e-f): MOOD-P2.

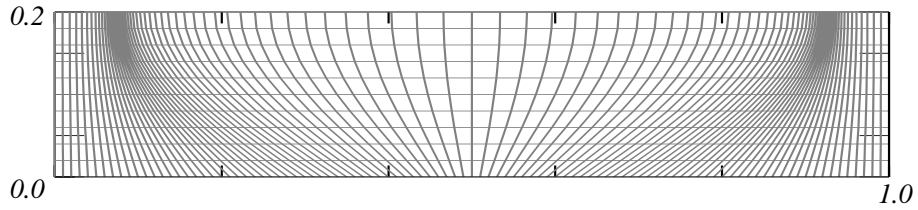


Fig. 11. Non-uniform mesh used for the Sod problem.

are represented so that the preservation of the 1D symmetry in the  $y$  direction can then be evaluated by the thickness of the points cloud. Clearly the MLP method provides the largest dispersion whereas the MOOD-P2 method manages to better preserve the  $y$  invariance. Such a test case suggests that the MOOD method is less sensitive to mesh deformation. As in the uniform case an undershoot at the tail of the rarefaction wave appears for MOOD-P2

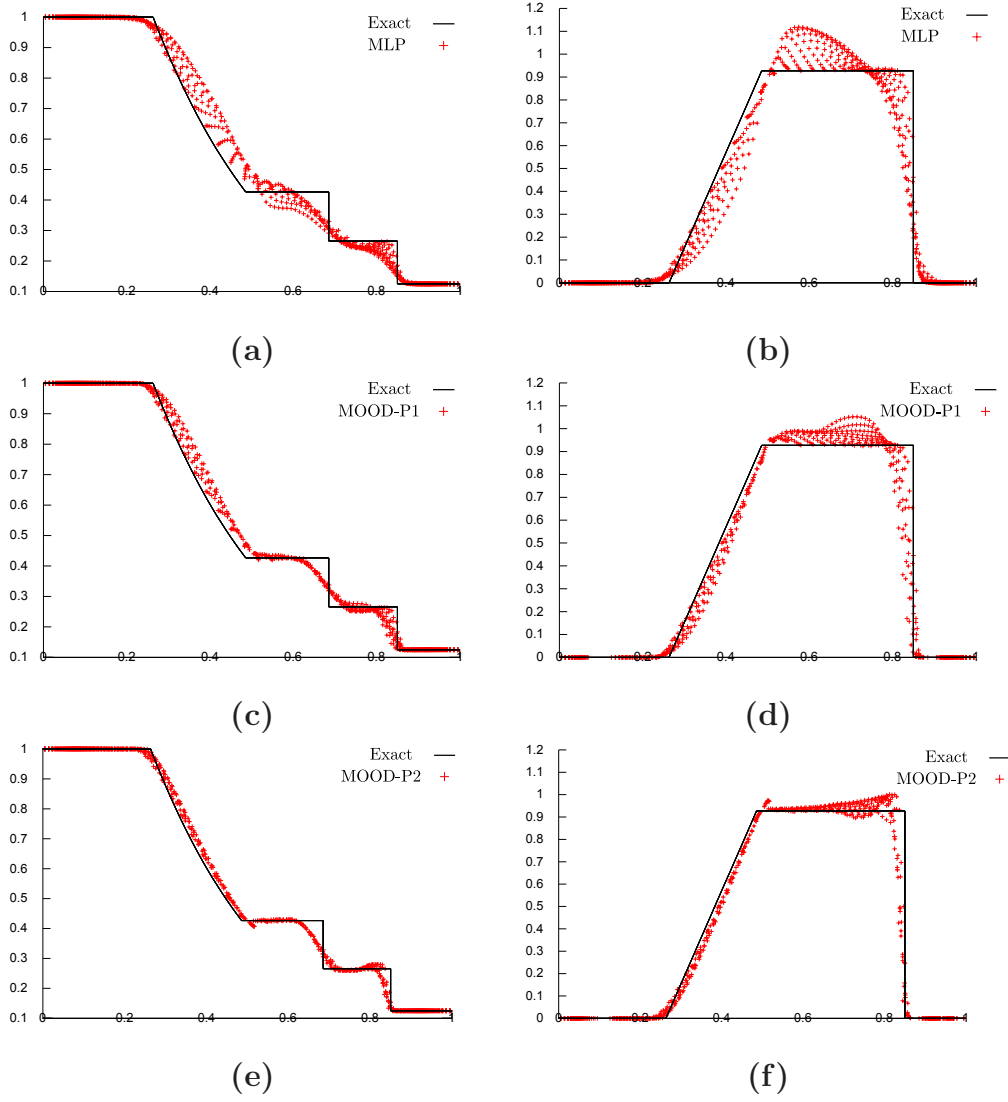


Fig. 12. Sod shock tube problem: Density and  $x$ -velocity on  $100 \times 10$  non-uniform mesh for (a-b): MLP — (c-d): MOOD-P1 — (e-f): MOOD-P2.

method but the solution is genuinely improved by comparison with MLP. The MOOD-P1 is an intermediate case we reduce the dispersion in comparison with the MLP method but we do not reach the MOOD-P2 accuracy. As expected we do not observe any under/overshoot with the MOOD method for the density variable.

## 7.2 Four states Riemann problem

We now deal with one of the four states Riemann problem initially proposed by [34] (see also [24]) which corresponds to a truly 2D Riemann problem. The computational domain  $\Omega = [0, 1] \times [0, 1]$  is uniformly meshed by a  $100 \times 100$  quadrangle grid. The four sub-domains correspond to four identical squares

separated by the lines  $x = 0.5$  and  $y = 0.5$ . Initial conditions on each sub domains are

- for the lower-left domain  $\Omega_{ll}$ :  $(\rho, u, v, p) = (0.029, 0.138, 1.206, 1.206)$ ,
- for the lower-right domain  $\Omega_{lr}$ :  $(0.3, 0.5323, 0, 1.206)$ ,
- for the upper-right domain  $\Omega_{ur}$ :  $(1.5, 1.5, 0, 0)$ ,
- for the upper-left domain  $\Omega_{ul}$ :  $(0.3, 0.5323, 1.206, 0)$ .

Each sub-domain is filled with a perfect gas of constant  $\gamma = 1.4$ . Reflective boundary conditions are prescribed and the computation is carried out till the final time  $t_f = 0.3$ .

Density at the final time is presented for the three methods in figures 13. For each figure on the left side one displays a three-dimensional elevation representation while in the right panels are plotted 30 isolines between the minimal density,  $\rho_m$ , and maximal one,  $\rho_M$  of each method.

The MLP method generates some oscillations on the plateau while the MOOD method better preserves the constant states. We obtain thinner shocks with the MOOD-P2 method and the central peak at  $x = y = 0.35$  is finer resolved which suggests that the method is more accurate.

We carry out the same simulation using the three methods but with a finer  $400 \times 400$  mesh and draw 30 density isolines in figure 14. The shock are finer with MOOD compared to MLP and the complex structures in the interaction area are better approximated with the MOOD-P2 method.

### 7.3 Mach 3 wind tunnel with a step

The test was initially proposed by [43]. A uniform Mach 3 flow enters in a tunnel which contains a 0.2 unit length step leading to a flow with complex structures of interacting shocks. The wind tunnel is 1 length unit wide and 3 length unit long and the step is located at 0.6 length unit from the left-hand side of the domain. At the initial time we consider a perfect gas ( $\gamma = 1.4$ ) with constant density  $\rho^0 = 1.4$ , uniform pressure  $p^0 = 1.0$  and constant velocity  $U^0 = (3, 0)$ . We prescribe reflective boundary conditions for the upper and lower sides while we set inflow boundary condition on the left side and an out-flow condition on the right side. Moreover, we prescribe symmetric boundary conditions in front of the step. Numerical simulations are carried out till the final time  $t_f = 4$ .

We plot a series of figures presenting 30 isolines of the density for three different uniform meshes on which the three methods are tested. We first consider the situation with coarse mesh using  $40 \times 120$  cells. Figures 15 represent the density computed with the MLP, the MOOD-P1 and MOOD-P2 methods respectively on top, middle and bottom panels. It is noticeable that the MOOD



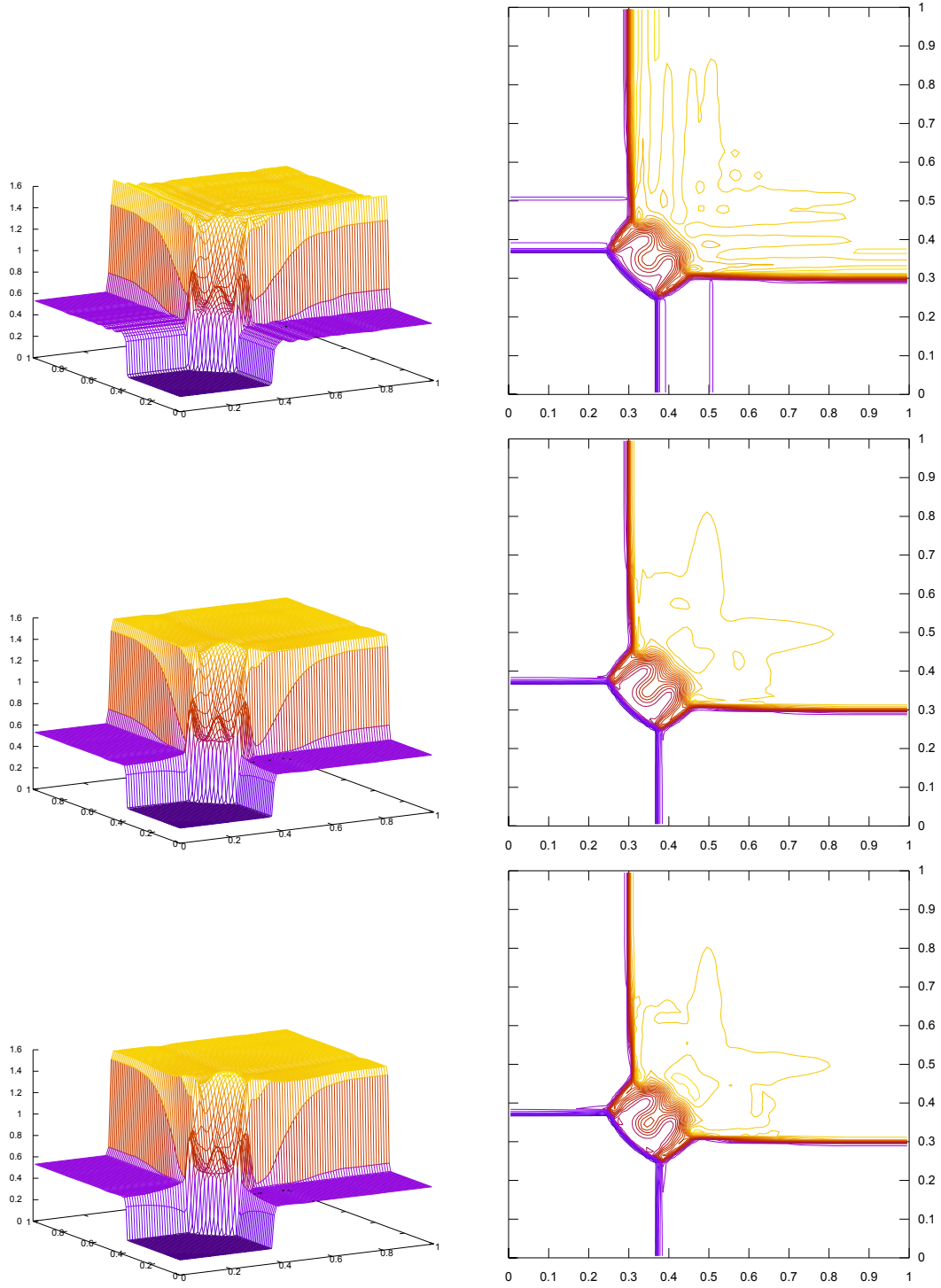


Fig. 13. Four states Riemann problem: Density on  $100 \times 100$  mesh — Left: 3D view, right: Corresponding 2D isolines — Top: MLP method  $\rho_m = 0.138$   $\rho_M = 1.57$  — Middle: MOOD-P1 method  $\rho_m = 0.138$   $\rho_M = 1.525$  — Bottom: MOOD-P2 method  $\rho_m = 0.1378$   $\rho_M = 1.541$ .

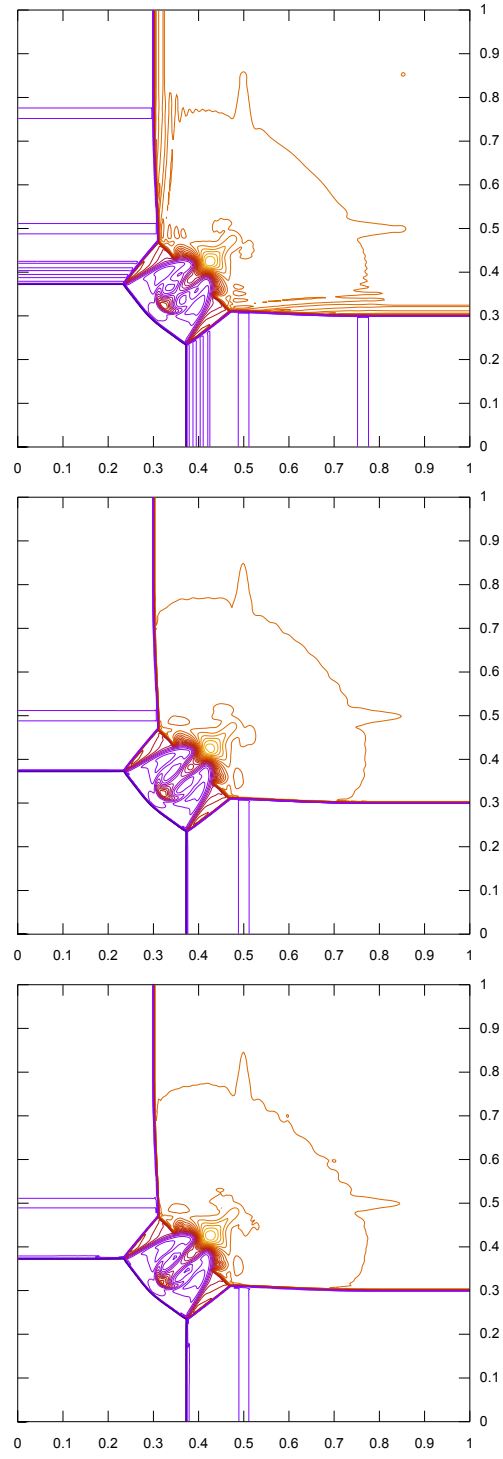


Fig. 14. Four states Riemann problem: Density on  $400 \times 400$  mesh — Top: MLP method  $\rho_m = 0.138$   $\rho_M = 1.821$  — Middle: MOOD-P1  $\rho_m = 0.1377$   $\rho_M = 1.805$  — Bottom: MOOD-P2  $\rho_m = 0.1379$   $\rho_M = 1.805$ .

method results are the most accurate. The shocks are less diffused and we can already observe the contact discontinuity formation of the upper slip line. With the MLP method, we remark that the formation of a triple point at  $x = 1.25$  above the step (at a distance of about 0.1) while the junction point should be exactly on the step interface. With the MOOD-P2 method, the triple point is closer to the interface (half the distance with respect to the MLP case).

We now plot the density obtained with finer meshes:  $80 \times 240$  cells (see figure 16) and  $160 \times 480$  cells (see figure 17). The mesh refinement provides more accurate solutions for any method. However the MOOD method always provides the best numerical approximation. An other noticeable fact is the formation of a triangle above the segment line defined by the step corner and the triple point. A slip line should appear starting at the step corner with an angle of about 30 degrees. Such a structure clearly appears with the MOOD method with an even more important effect for the MOOD-P2 reconstruction. At last the upper slip line located at  $y = 0.8$  is sharper and can be seen across the whole domain. However the method does not reveal the Kelvin-Helmholtz instability as in [14] as the strict DMP on the density reduces the scheme accuracy along the slip line and consequently increases the numerical dissipation.

#### 7.4 *Double Mach reflection of a strong shock*

The last problem is the double mach reflection of a strong shock proposed in [43]. This test problem involves a Mach 10 shock which initially makes a  $60^\circ$  angle with a reflecting wall. The air ahead of the shock is at rest and has uniform initial density  $\rho^0 = 1.4$  and pressure  $P^0 = 1$ . A perfect equation of state with  $\gamma = 1.4$  is considered. The reflecting wall lies along the bottom of the domain, beginning at  $x = l/6$ . The shock makes a 60 degrees angle with the  $x$  axis and extends to the top of the domain at  $y = 1$ . The short region from  $x = 0$  to  $x = l/6$  along the bottom boundary at  $y = 0$  is always assigned values for the initial post-shock flow. We prescribe a reflective condition on the bottom part for  $x > l/6$ , Dirichlet condition (supersonic inflow condition) on the left side and outflow condition on the right side. At the top boundary, the boundary conditions are set to describe the exact motion of the Mach 10 flow (see also [14]).

Results are presented with isolines on a top view of 30 isolines of density plotted between minimal and maximal values taken over the results of the three methods on the same mesh. Mesh refinement is done by dividing by two the characteristic length starting with a  $80 \times 320$  mesh up to a  $480 \times 1920$  mesh. Results are presented in figures 18-19-20 for MLP method (top panels), in figures 18-19-20 for MOOD-P1 method (middle panels) and in figures 18-

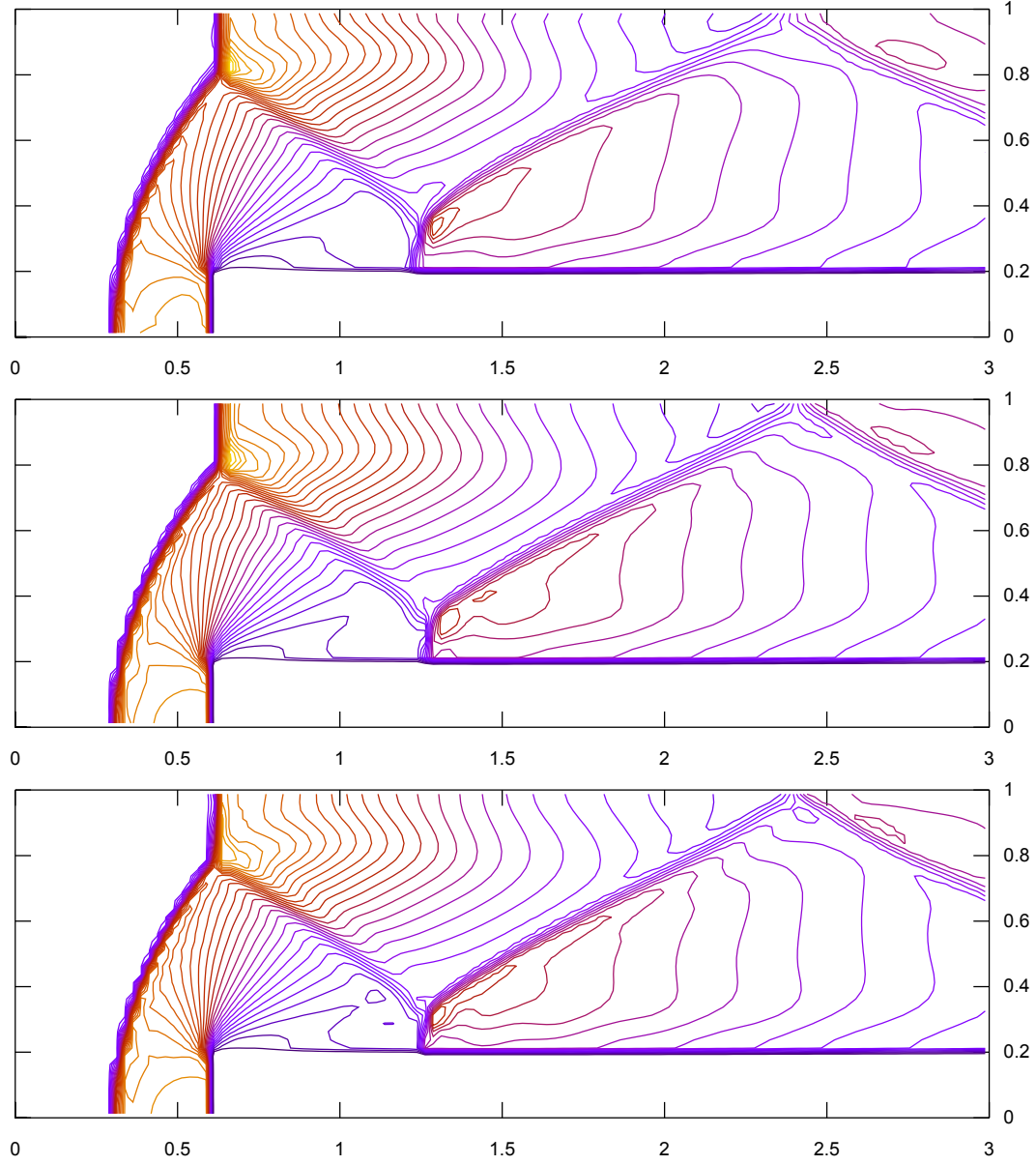


Fig. 15. Mach 3 problem — Density with 30 isolines between min and max on  $40 \times 120$  mesh, Top: MLP method  $\rho_m = 0.5437$   $\rho_M = 6.75$  — Middle: MOOD-P1 method  $\rho_m = 0.5589$   $\rho_M = 6.58$  — Bottom: MOOD-P2 method  $\rho_m = 0.5358$   $\rho_M = 6.047$ .

19-20 for MOOD-P2 method (bottom panels). Zoom on the right part of the domain is displayed in figure 21 with 50 isolines of density plotted between minimal and maximal values in order to emphasize tiny details of the solution.

The first Mach stem M1 is connected to the main triple junction point with the incident shock wave and the reflected wave. A slip line is generated from the triple junction point behind the incident shock. A secondary Mach stem M2 also appear and interact with the slip line. Using a coarse mesh, the MOOD-P2 manages to better capture the Mach stem M1 with respect to the two other methods and this point is confirmed and also available for the secondary

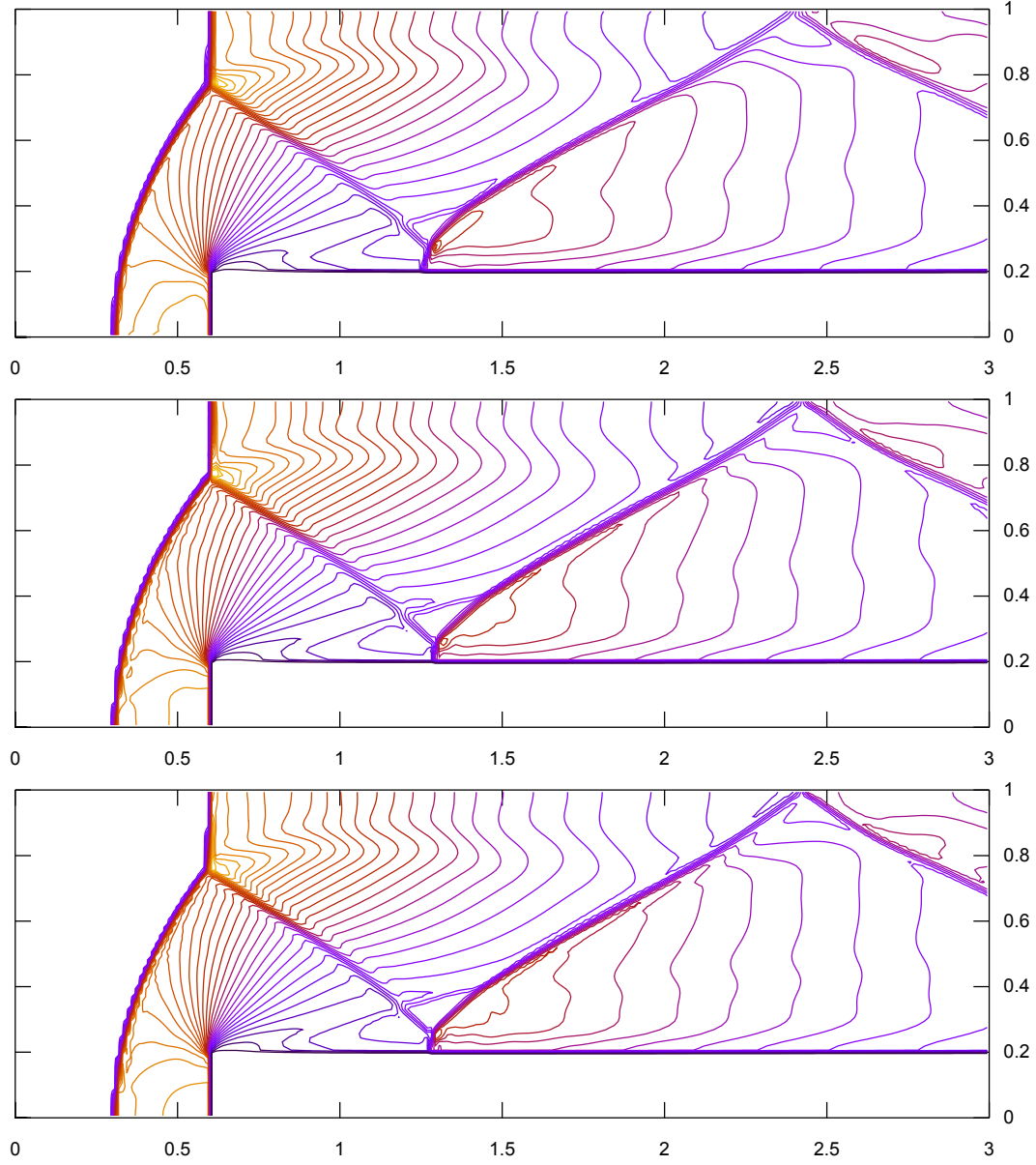


Fig. 16. Mach 3 problem — Density with 30 isolines between min and max on  $80 \times 240$  mesh, Top: MLP method  $\rho_m = 0.313$   $\rho_M = 6.489$  — Middle: MOOD-P1 method  $\rho_m = 0.329$   $\rho_M = 6.628$  — Bottom: MOOD-P2 method  $\rho_m = 0.337$   $\rho_M = 6.412$ .

Mach stem M2 when we employ finer meshes. The slip line corresponds to a contact discontinuity where the jump of tangential velocity may generate Kelvin Helmholtz instabilities. Usually, the amount of instability measures the numerical diffusion impact [31]: large instabilities derive from small numerical diffusion and the number of plane vortexes in the slip line is a qualitative measure of the scheme diffusivity. In our test, even with the finest mesh, no instability is reported. Indeed, the application of a strict DMP reduces the accuracy of the scheme in the vicinity of the slip line maintaining a too large amount of diffusion. In the WENO framework, the strict DMP property

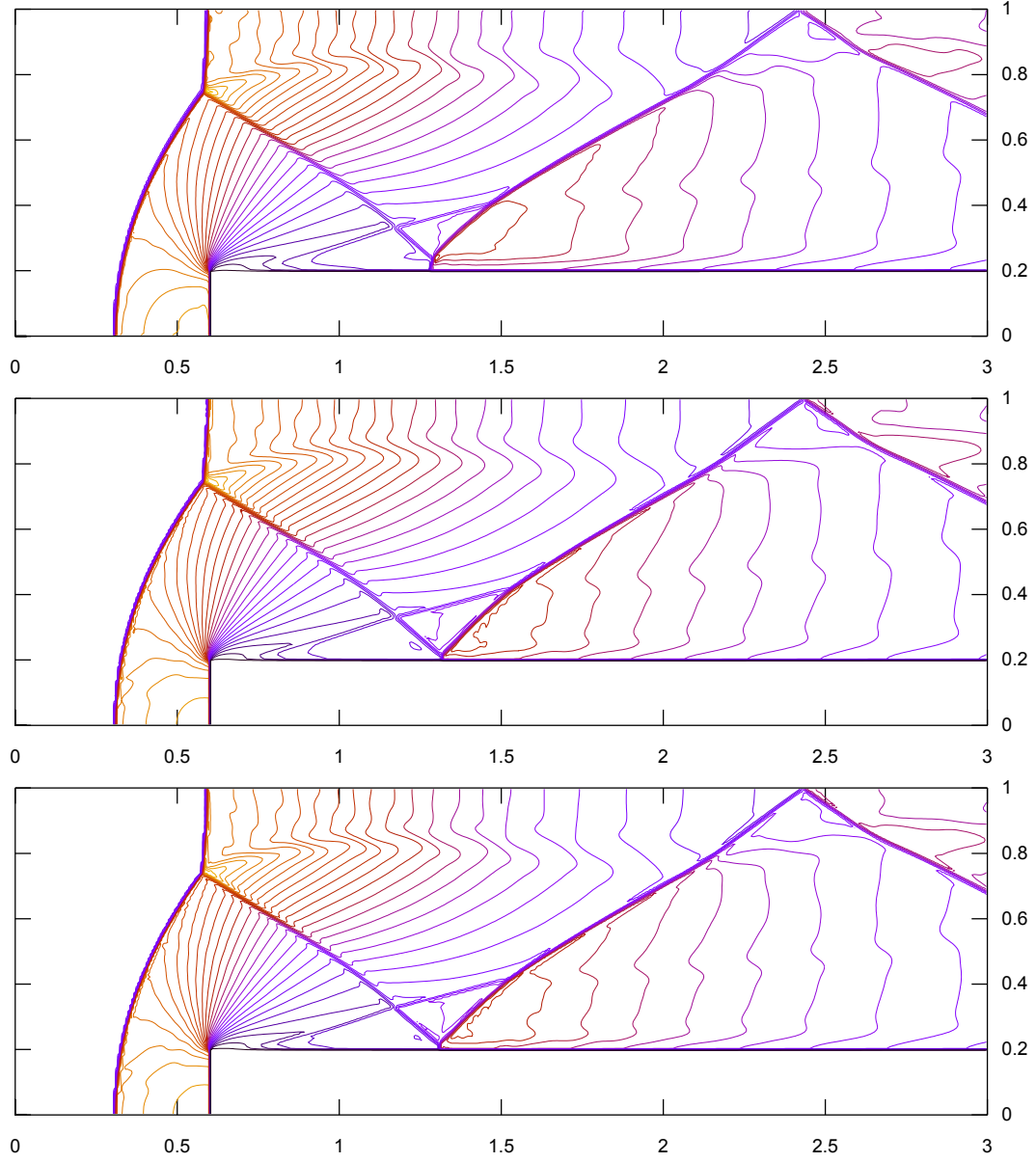


Fig. 17. Mach 3 problem — Density with 30 isolines between min and max on  $160 \times 480$  mesh, Top: MLP method  $\rho_m = 0.176$   $\rho_M = 6.802$  — Middle: MOOD-P1 method  $\rho_m = 0.150$   $\rho_M = 6.483$  — Bottom: MOOD-P2 method  $\rho_m = 0.123$   $\rho_M = 6.257$ .

is not achieved and numerical diffusion is strongly reduced but non-physical instabilities might appear in that case. Nevertheless, other choices of detection variables would be investigated to reduce the numerical diffusion for contact discontinuities.

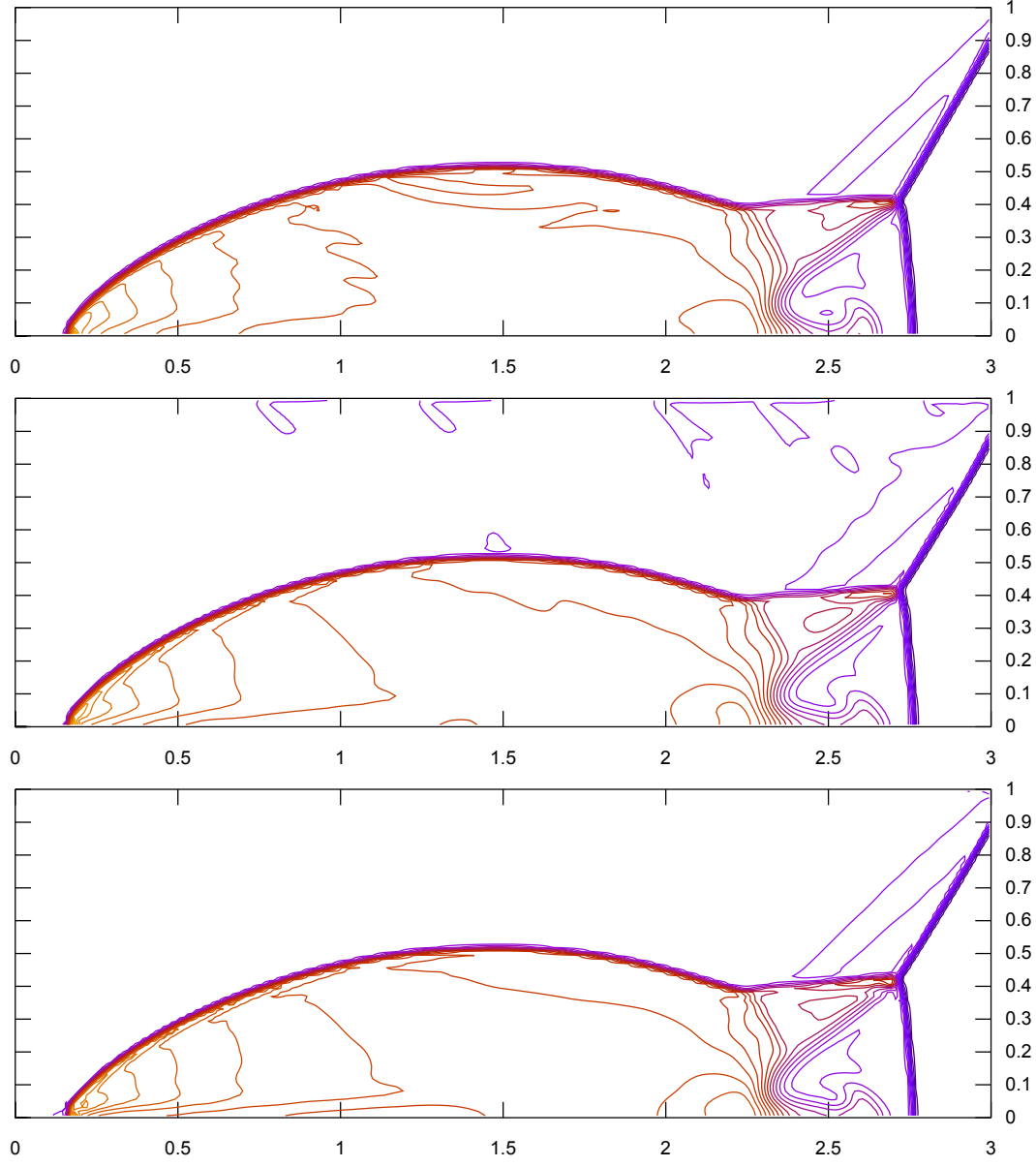


Fig. 18. Double Mach problem on 80x320 Top: MLP method  $\rho_m = 1.400$   $\rho_M = 23.200$  — Middle: MOOD-P1 method  $\rho_m = 1.280$   $\rho_M = 22.460$  — Bottom: MOOD-P2 method  $\rho_m = 1.228$   $\rho_M = 21.680$ .

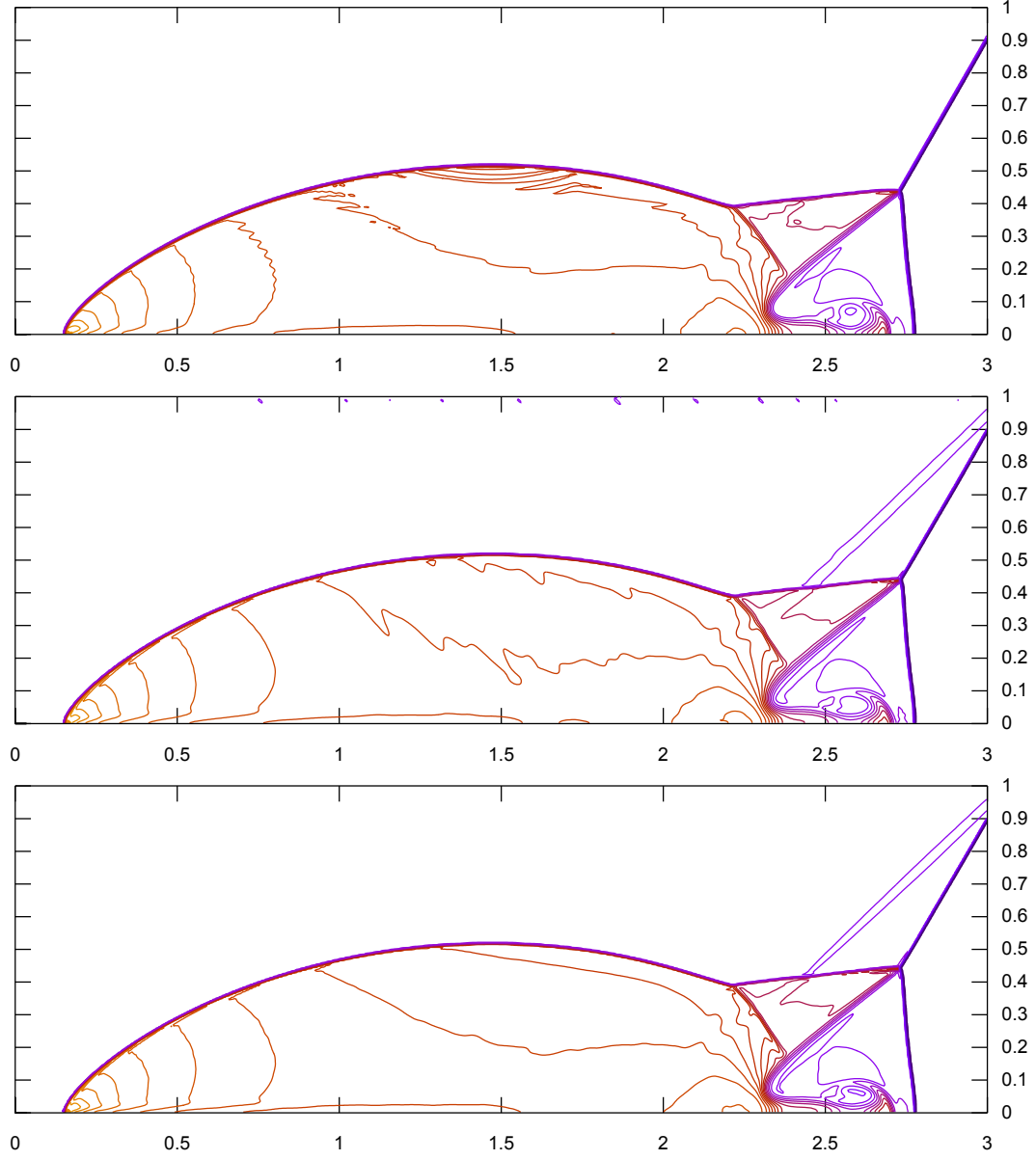


Fig. 19. Double Mach problem on 240x960 — Top: MLP method  $\rho_m = 1.400$   $\rho_M = 22.400$  — Middle: MOOD-P1 method  $\rho_m = 1.236$   $\rho_M = 22.550$  — Bottom: MOOD-P2 method  $\rho_m = 1.162$   $\rho_M = 22.800$ .



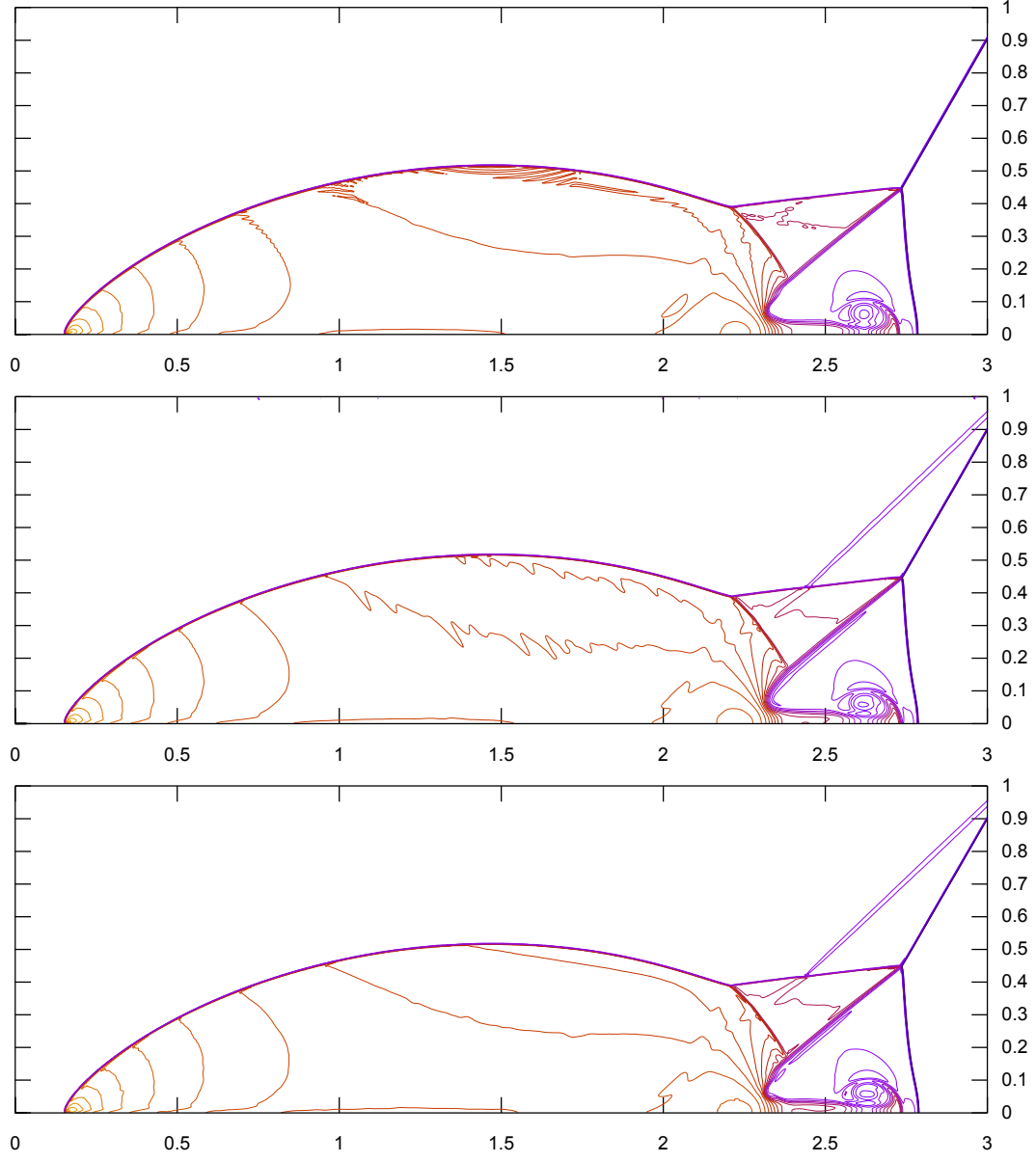


Fig. 20. Double Mach problem on 480x1920 — Top: MLP method  $\rho_m = 1.400$   $\rho_M = 22.68$  — Middle: MOOD-P1 method  $\rho_m = 1.216$   $\rho_M = 22.0$  — Bottom: MOOD-P2 method  $\rho_m = 1.146$   $\rho_M = 21.99$ .

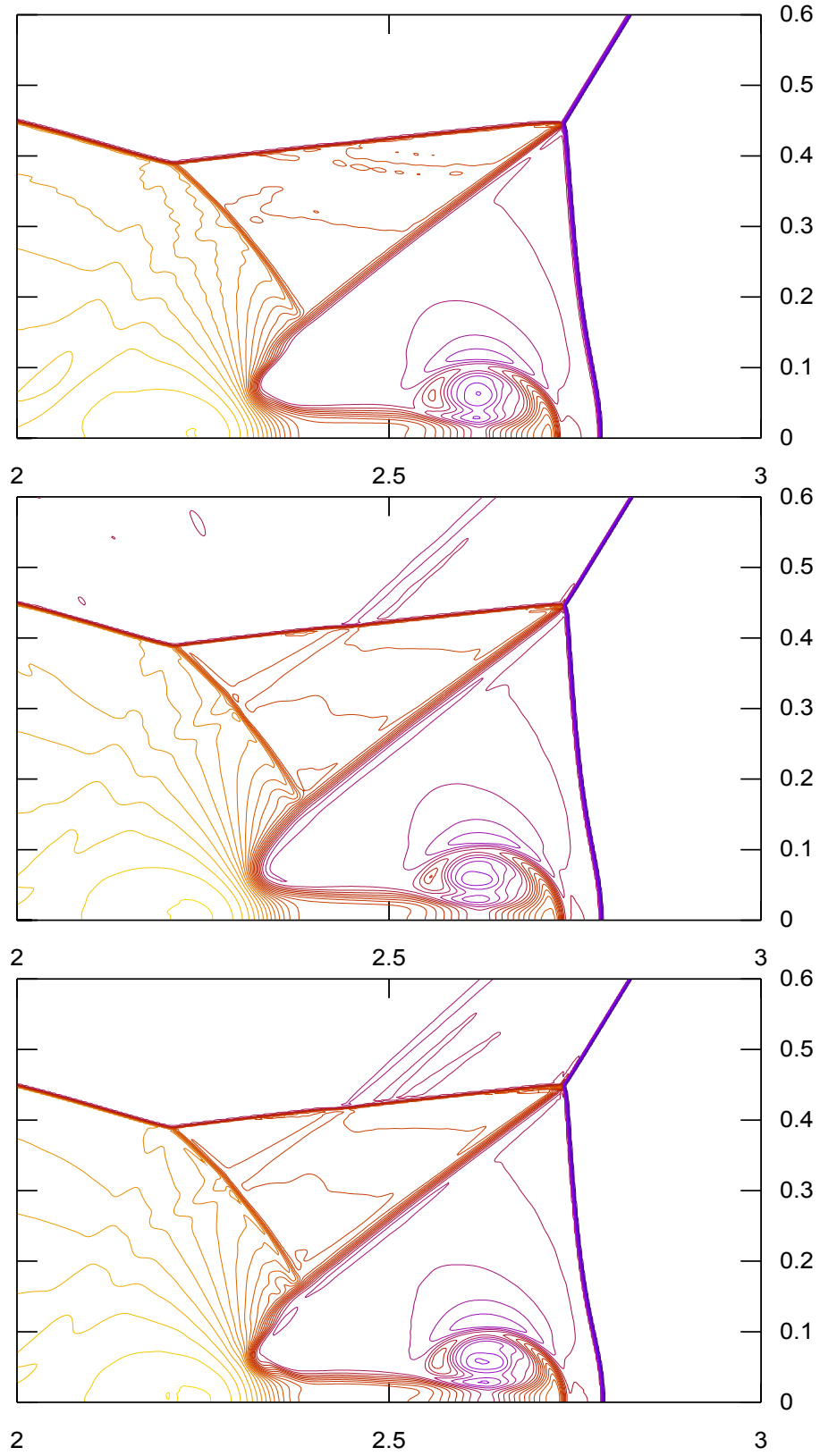


Fig. 21. Double Mach problem on 480x1920 — Zoom on the wave interaction zone — Top: MLP method  $\rho_m = 1.400$   $\rho_M = 22.68$  — Middle: MOOD-P1 method  $\rho_m = 1.216$   $\rho_M = 22.0$  — Bottom: MOOD-P2 method  $\rho_m = 1.146$   $\rho_M = 21.99$ .

## 8 Conclusion and perspectives

This paper presents a very high-order polynomial finite volume method for hyperbolic system of conservation laws with Multi-dimensional Optimal Order Detection (MOOD) in an Eulerian framework. Unlimited polynomial reconstructions of state variables are used in a classical finite volume scheme. Eventually the polynomial degree is reduced in the cell neighborhood for which the Discrete Maximum Principle is not fulfilled. A “corrected” approximate solution is reconstructed using the reduced degree polynomials. This procedure is repeated up to satisfaction of the Discrete Maximum Principle. Instead of designing an *a priori* limiter as for classical high-order methods one reduces the polynomial degree *a posteriori*. The iterative decrementing procedure is in fact embedded in the sub-steps of a Runge-Kutta scheme leading to a high-order time discretization. An extension of MOOD to Euler system is presented; the polynomial degree reduction is performed if either the density does not fulfill the Discrete Maximum Principle or the pressure is non positive.

Two-dimensional numerical results are provided for the advection equation and the Euler system of conservation laws on quadrangular regular and highly non-regular meshes for second- and third-order accurate MOOD schemes. We proved that the MOOD method can reach optimal order of accuracy on smooth and non-regular meshes for advection of various shapes. Then we showed with the two-dimensional Sod shock tube that MOOD still performs very well on non-regular mesh. Finally we proved the good behavior of MOOD on the four states Riemann problem, Mach 3 step and double Mach reflection problems. This paper is the first one presenting the MOOD concept. Consequently several behaviors and extensions demand for more investigations. As instance we plan to investigate more deeply new Edge Polynomial Degree (EPD) strategies that could eventually adapt and act with less abrupt changes. Moreover we plan to study the behavior of the MOOD concept with polynomials of degree greater than two and polygonal/polyhedral meshes. Finally no special treatment should theoretically be provided for the concept and the *a posteriori* limitation to be effective.

## References

- [1] R. Abgrall On Essentially Non-oscillatory Schemes on Unstructured Meshes: Analysis and Implementation J. Comput. Phys. 114 (1994) 45–58.
- [2] R. Abgrall, Essentially non-oscillatory Residual Distribution schemes for hyperbolic problems J. Comput. Phys. 214 (2006) 773–808.
- [3] T. J. Barth, Numerical methods for conservation laws on structured and unstructured meshes, VKI March 2003 Lectures Series.
- [4] T. J. Barth, D. C. Jespersen, The design and application of upwind schemes on unstructured meshes, AIAA Report 89-0366, 1989.
- [5] G. Capdeville, A central WENO scheme for solving hyperbolic conservation laws on non-uniform meshes J. Comput. Phys., Vol 227, 2008
- [6] T. Buffard, S. Clain, Monoslope and Multislope MUSCL Methods for unstructured meshes, J. Comput. Phys. 229 (2010) 3745–3776.
- [7] R.L. Carpenter, K. Droegemeier, P.R. Woodward, C.E. Hane, Application of the Piecewise Parabolic Method (PPM) to meteorological modeling, Monthly Weather Review, 118, 586–612, (1989)
- [8] S. Clain, Finite volume  $L^\infty$ -stability for hyperbolic scalar problems, preprint HAL available at <http://hal.archives-ouvertes.fr/hal-00467650/fr/>.
- [9] S. Clain, V. Clauzon,  $L^\infty$  stability of the MUSCL methods, Numer. Math. 116, 31–64, (2010).
- [10] I. Christov, B. Popov, New non-oscillatory central schemes on unstructured triangulations for hyperbolic systems of conservation laws, J. Comput Phy. 227 (2008) 5736–5757.
- [11] B. Cockburn and C. W. Shu, TVB Runge-Kutta local projection previous term discontinuous Galerkin finite element method for scalar conservation laws II: General framework. Math. Comp. 52 (1989), p. 411.
- [12] B. Cockburn, S. Y. Lin and C. W. Shu, TVB Runge-Kutta local projection previous term discontinuous Galerkin finite element method for conservation laws III: One dimensional systems. J. Comput. Phys. 84 (1989), p. 90.
- [13] B. Cockburn, S. Hou and C. W. Shu, TVB Runge-Kutta local projection previous term discontinuous Galerkin finite element method for conservation laws IV: The multidimensional case. Math. Comp. 54 (1990), p. 545.
- [14] B. Cockburn, C.-W. Shu, The Runge-Kutta Discontinuous Galerkin Method for Conservation Laws V: Multidimensional Systems J. Comput. Phys. 141 (1998) 199–224.
- [15] P. Colella and P.R. Woodward, The Piecewise Parabolic Method (PPM) for Gas-Dynamical Simulations, J. Comput. Phys. 54, 174–201 (1984)

- [16] A. Csík, M. Ricchiuto, H. Deconinck, A Conservative Formulation of the Multidimensional Upwind Residual Distribution Schemes for General Nonlinear Conservation Laws, *J. Comput. Phys.*, 179 (2002) 286–312.
- [17] M. Dumbser, M. Castro, C. Pars, E. F. Toro ADER schemes on unstructured meshes for nonconservative hyperbolic systems: Applications to geophysical flows *Computers and Fluids*, 38 (2009) 1731–1748.
- [18] R. Harris, Z. J. Wang, Y. Liu, Efficient quadrature-free high-order spectral volume method on unstructured grids: Theory and 2D implementation, *J. Comput. Phys.*, 227 (2008) 1620–1642.
- [19] A. Harten and S. Osher, Uniformly highorder accurate nonoscillatory schemes I, *SIAM J. Num. Anal.* , 24, (1987) 279309.
- [20] A. Harten, B. Engquist, S. Osher and S. Chakravarthy, Uniformly highorder accurate nonoscillatory schemes III, *J. Comput. Phys.*, 71, (1987) 279309.
- [21] M. E. Hubbard, Multidimensional slope limiters for MUSCL-type finite volume schemes on unstructured grids, *J. Comput. Phys.* 155 (1) (1999) 54–74.
- [22] G.-S. Jiang, C.-W. Shu, Efficient implementation of weighted ENO schemes *J. Comput. Phys.*, 126 , (1996) 202–228.
- [23] Randall J. Leveque High-Resolution Conservative Algorithms for Advection in Incompressible Flow, *SIAM J. Num. Anal.* , 33 (1996) 627-665.
- [24] R. Liska, B. Wendroff Comparison of several difference schemes on 1D and 2D test problems for the Euler equations. *SIAM J. Sci. Comput.*, 25 (2003) 995-1017
- [25] P.R.M. Lyra, K. Morgan, A Review and Comparative Study of Upwind Biased Schemes for Compressible Flow Computation. Part II: 1D HigherOrder Schemes, *Archives of Computational Methods in Engineering*, Vol. 7, 3, 333-377 (2000)
- [26] C. F. Ollivier-Gooch Quasi-ENO Schemes for Unstructured Meshes Based on Unlimited Data-Dependent Least-Squares Reconstruction, *J. Comput. Phys.*, 133 (1997) 6–17.
- [27] J. S. Park, S.-H. Yoon, C. Kim, Multi-dimensional limiting process for hyperbolic conservation laws on unstructured grids, *J. Comput. Phys.* 229 (2010) 788–812.
- [28] M. Ricchiuto, A. Bollermann, Stabilized residual distribution for shallow water simulations *J. Comput. Phys.*, 228 (2009) 1071–1115.
- [29] P. Roe, Characteristic-based schemes for the Euler equations, *Ann. Rev. Fluid Mech.*, 18 (1986) 337–.
- [30] A. Rogertson, E. Meiburg, A numerical study of the convergence of ENO schemes, *J. Sci. Comput.* 5 (1990) 151167.
- [31] J. Shi, Y-T Zhang, C-W Shu, Resolution of high order WENO schemes for complicated flow structures, *J. comput. phys.* 186 (2003) 690–696.

- [32] C.-W. Shu, High order weighted essentially nonoscillatory schemes for convection dominated problems, SIAM Review, Vol. 51, No 1 (2009) 82–126.
- [33] C.-W. Shu, S. Osher, Efficient implementation of essentially non-oscillatory shock-capturing scheme, J. Comput. Phys., 77 (1988) 439–471.
- [34] C. W. Schulz-Rinne, J. P. Collins, and H. M. Glaz. Numerical solution of the Riemann problem for two-dimensional gas dynamics. SIAM J. Sci. Comput., 14:13941414, 1993.
- [35] V.A. Titarev, E.F. Toro, ADER schemes for three-dimensional non-linear hyperbolic systems J. Comput. Phys. 204 (2005) 715–736.
- [36] E. F. Toro Riemann Solvers and Numerical Methods for Fluid Dynamics Springer.
- [37] E. F. Toro, A. Hidalgo ADER finite volume schemes for nonlinear reactiondiffusion equations, Applied Numerical Mathematics, 59 (2009) 73–100.
- [38] Van Albada, G D, B. Van Leer and W. W. Roberts, A comparative study of computational methods in cosmic gas dynamics, Astron. Astrophysics, 108, (1982), p76.
- [39] B. Van Leer, Towards the ultimate conservative difference scheme II. Monotonicity and conservation combined in a second order scheme. J. Comp. Phys., 14, (1974), p361-70.
- [40] Z. J. Wang, Spectral (finite) volume method for conservation laws on unstructured grids: basic formulation, J. Comput. Phys. 178 (2002) 210–251.
- [41] Z. J. Wang, Y. Liu Spectral (finite) volume method for conservation laws on unstructured grids: extention to two dimensional scalar equation, J. Comput. Phys. 179 (2002) 665–697.
- [42] W. R. Wolf , J. L. F. Azevedo, High-order ENO and WENO schemes for unstructured grids, International Journal for Numerical Methods in Fluids, 55 Issue 10 (2007) 917—943
- [43] P. Woodward, P. Colella, The numerical simulation of two-dimensional fluid flow with strong shocks, J. Comput. Phys. 54 (1984) 115173.
- [44] Y.-T. Zhang and C.-W. Shu Third order WENO scheme on three dimensional tetrahedral meshes. Com. Comput. Phys., 5 (2009) 836–848.